Enhanced dual threshold detection method enabling fast and robust primary wave time range estimation

Jakob Harden[1]

October 11, 2025

Abstract

The ultrasonic pulse transmission method is a well-established non-destructive testing technique in industry and research. The analysis of the resulting signal data typically aims to determine the time range, as this allows for estimating the speed of sound, a crucial material property. One of the fundamental methods to estimate the time range is threshold detection. Unfortunately, the detection results are biased due to the shape of the signal and the chosen threshold value. In the existing literature, several approaches to reducing this bias are present. The a posteriori signal processing method presented in this paper is based on a threshold detection method with two thresholds and automatic error correction, as described in the literature. However, it also introduces several modifications to enhance the method's robustness concerning frequency and noise. These mainly consist of threshold value optimisation and systematic error correction by taking into account the signal's shape in the detection zone. The analysis results, based on synthetic and natural signals, clearly demonstrate that the proposed method remarkably reduces the residual detection error while requiring moderate computational effort. Since this method does not involve filtering, noise is the governing factor limiting its application range. A comparison of different method variants with methods adapted from literature shows that the proposed method is fast, robust and outperforms the literature-based methods, especially in the regime of low frequencies and increasingly dominant noise.

[1]Graz University of Technology, Faculty of Civil Engineering Sciences, Institute of Technology and Testing of Construction Materials, Inffeldgasse 24/I, 8010 Graz, Austria; Corresponding author email: jakob.harden@tugraz.at

1 Introduction

Over the past few decades, the ultrasonic pulse transmission method (UPTM) has established itself as a pivotal testing technique in the field of non-destructive testing[1–4]. In industry, this technique is mainly used for distance and flow measurements[5,6], as well as product quality assurance[7,8]. This testing technique is of utmost importance in cases where invasive testing methods are undesirable or are not applicable due to the physical state of the material being tested. For this reason, this testing technique has established itself as a state-of-the-art technique[9], particularly for testing gaseous, liquid and paste-like materials.

The functional principle of the UPTM using piezoelectric transducers consists of the mechanical excitation of the test specimen, the propagation of the sound wave through the test specimen and the observation of the arriving sound wave at a specific distance from the sound source. The period between the moment of excitation of the test specimen and the moment of observation of the incoming sound wave is referred to as the sound travel time, time range or time-of-flight. However, the time range and the ultrasonic measuring distance, which is the distance between the sound source and the observation point, determine the speed of sound. It is worth mentioning that the determination of the speed of sound is of particular importance, as it represents an important material property.

Problem statement. When estimating the speed of sound of a material, the key problem is to determine the time range as accurately as possible. Due to the characteristics of the sound wave, this can be challenging. The signal response of the incoming sound wave, typical for the UPTM, is a damped, harmonic oscillation superimposed by additive noise. Particularly problematic is the fact that the signal amplitudes of the incoming sound wave do not rise abruptly, but begin with very small amplitudes in the noise floor rather than as a visually recognisable signal curve. Therefore, the primary wave's onset point, which determines the time range, is located in the noise floor and thus difficult to locate.

Literature. The relevant literature provides several digital signal processing methods[10,11], which can also be implemented in the hardware of an ultrasonic testing device[12–14]. Hardware implementations retain the advantage that the time range can be estimated in quasi-real-time and are therefore well suited for online controlling production processes. The costs and functional scope of the hardware are limiting factors for the accuracy of the time range estimates. For sampled signals (discrete-time signals), computer-aided signal processing is the option offering the broadest range of opportunities for the analysis. But it comes with the disadvantage that signal analysis takes place after signal recording and may return the analysis results with a considerable time delay.

Due to its universal applicability and simplicity, threshold detection is one of the most commonly used signal processing methods in the field of ultrasound signal analysis[13,15–18]. The disadvantage of this method is that the time range is generally biased (overestimated), which is mainly related to the chosen threshold value and the shape of the signal. Due to noise, choosing an appropriate threshold value can be challenging and is the leading cause of false detections. Other

methods, such as correlation analysis and wavelet analysis, are more robust to noise but cause a considerably greater computational effort.

In a paper[15] by Piyush et al. (2023), an experimental device is described whose signal processing method is based on threshold detection performed twice in succession (dual threshold detection). The signal indices determined from the dual threshold detection are the supports of a straight line whose intersection with the time axis (x-axis crossing) provides the corrected estimate of the signal's onset point. It is worth mentioning that in this method the threshold detection is applied to the envelope of the signal instead of the signal itself.

Another interesting double-threshold detection method is presented in a paper[18] of Barshan (2000). The method is based on a Dirichlet window of given length shifted along the signal until a predefined proportion (first threshold) of signal amplitudes within the sliding window exceeds a predefined voltage (second threshold). When this detection condition is satisfied, the window shift supplies the estimate onset point of the sound wave. That method is also employed in the electronic circuit design of an optimised two-path ultrasonic flow-meter for gaseous media proposed in a paper[13] by Weihua et al. (2014).

Solution approach. This work goes one step further by taking into account the special shape of natural ultrasound signals in the range between the onset point and the first local maximum of the primary wave's signal response – the detection zone. Similar to the approach[15] of Piyush et al. (2023), the detection approach presented is this paper is based on dual threshold detection, but additionally introduces systematic error correction. The constituent elements of the solution approach are:

- **Choice of a coherent signal model** that fits well to natural signals within the detection zone.
- **Optimisation of the detection parameters** (threshold values) concerning the signal model.
- **Normalisation of the signal amplitudes** to the primary wave's first local maximum. That allows for using constant threshold values, independent of the signal's actual amplitude.
- **Dual threshold detection** with optimised detection parameters delivering the support for a secant used to replace the signal within the detection zone. The secant line's x-axis crossing supplies a first, but still biased, estimate for the primary wave's onset point location.
- **Systematic error correction** by adding a correction value, which is related to the secant line's gradient.

A brief overview about the functional principle of the proposed signal processing methods is illustrated in Fig. 1, p. 5.

Design goals. The main design goals of the solution approach are ease of use, low complexity, improved accuracy and precision, and maximum robustness to frequency and noise. Signal filtering is not intended, as it is associated with a phase shift, which could slant the signal curve and thus be disadvantageous when estimating the time range. To reduce the impact of noise, instead, linear

regression is employed to estimate the secant to the signal within the detection zone.

Improvements. The solution approach relies on a set of well-known and straightforward techniques of classic signal analysis. Solely the innovative combination of these techniques allows for the improvement in robustness, complexity, accuracy and precision. The most important enhancements compared to the literature are the detection parameter optimisation and the systematic error correction based on the shape of a signal model, which corresponds to the shape of ultrasound signals. To demonstrate the improvement, the above-described solution approach is compared with two literature-based time range estimation methods[15,18]. To provide fair comparison conditions, that methods are adapted to the chosen signal model as well.

Applicability domains. The time range estimation methods emerging from the solution approach are primarily designed for the a posteriori analysis of signal responses from compression waves (primary waves) originating from ultrasound tests using the UPTM. The explanations in this paper are therefore foremost related to this type of signals. However, it is demonstrated that these methods apply to signal responses related to different testing materials (cement paste, ambient air, tap water, aluminium cylinder).

Apart from this, the method's dominating prerequisite is a predominantly monotonically ascending flank within the detection zone. That prerequisite is not only satisfied by ultrasonic signals originating from the UPTM. Similar behavioural patterns can be observed in signals from the ultrasonic pulse reflection method, in ramp signals, sawtooth signals or exponential signals. It is therefore quite likely that the method's application scope, when choosing an appropriate signal model, extends well beyond the limits of the ultrasound signals used in this paper.

Content of this paper. This work is designed as a method paper. Therefore, the materials (synthetic and natural signals), the fundamental analysis methods, the enhanced detection methods, and the comparison methods derived from literature are described in detail. Natural signals are used to demonstrate that the presented detection methods are not limited to synthetic test signals used to investigate the method's performance. However, material properties of the testing materials related to those signals are not discussed in this paper.

The story of this paper starts with fitting an appropriate synthetic signal model to natural signals. That allows for showing that the signal model adapts well to a variety of natural signals originating from UPTM tests. Based on that, the method's detection parameters are optimised concerning the signal model's shape. The optimised detection parameters prepare the floor for investigating the method's properties concerning the signal model by performing a sensitivity analysis. The detection error statistics derived from the sensitivity analysis allow for assessing the method's robustness to frequency and noise, as well as its complexity, accuracy, and precision. After that, the story shifts its place of action towards natural signals. That is to show that the analysis methods also apply to natural signals originating from UPTM tests and not just to a theoretical signal model. The following discussion of the analysis result compares the

methods in terms of robustness and performance. Furthermore, exceptional or unexpected behaviour is highlighted and explained. The story ends with a conclusion of the most important findings and an outlook for future development and improvement potentials.

Code availability. To foster the comprehensibility and reliability of the presented analysis results, it is imperative to allow for their reproduction. Therefore, the entire program code[30] and all data required to reproduce the analysis results, as well as the analysis results[31], are made available under the GNU Affero General Public license the MIT license and the Creative Commons Attribution 4.0 International license. Furthermore, references to the GNU Octave (version 6.2.0) function files containing the realisations of the presented algorithms, are provided throughout this paper. Publishing the materials related to this paper aims to facilitate and accelerate the development of signal analysis methods related to the ultrasound testing technique. It is, furthermore, a visible sign of the author's spirit and commitment to the UNESCO Open Science Recommendations.

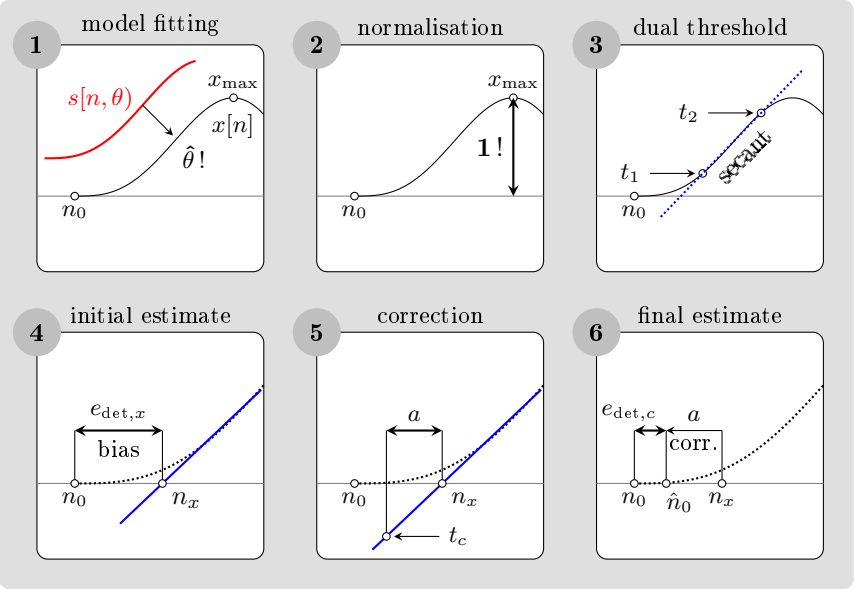

Figure 1: Functional principle of the primary wave onset point detection and error correction. *Legend:* $s[n,\theta)$ ... signal model; $x[n]$ ... natural signal; $\max_1$ ... first local maximum; n_0 ... exact onset point; t_1, t_2, t_c ... optimised threshold values; n_x ... biased onset point estimate; a ... error correction amount; $\hat{n}_0$ ... corrected onset point estimate; $e_{\mathrm{det},x}$, $e_{\mathrm{det},c}$ ... residual detection errors.

2 Materials & Methods

The introduction already outlined the basic principles and design objectives of the signal processing methods. First, the materials, consisting of synthetic and

natural signals, are described. Second, the fundamental methods forming the basis of the proposed onset point detection methods are explained. Third, the enhanced detection methods, comparison methods motivated by literature[15,18], and the optimisation of their parameters are detailed. Fourth, the performance standards and metrics to measure the method's properties are defined. The section closes with a description of the procedural steps to compile the analysis results presented in the results section of this paper.

2.1 Materials

The analyses in this paper rely on damped sinusoidal synthetic signals and natural signals from laboratory experiments using the UPTM. Synthetic signals help to optimise threshold values, to measure the processing error and to examine the method's properties. Natural signals allow for demonstrating that the proposed signal processing methods apply to natural signals as well. Since this paper exclusively deals with discrete, equidistantly sampled time signals $s(t, \theta)$, the time t is replaced with the sample index n, which yields the discrete formulation $s[n, \theta)$.

Synthetic signals. The signal model for synthetic signals employs the components of the solution to the differential equation of a damped mass-spring oscillator, which consist of the sine function and the exponential function. This mechanical model provides a reasonable approximation for the oscillation behaviour of piezoelectric elements excited by an exponentially decaying pulse. The signal model and its parameters are selected such that it adapts with a small error to the first ascending flank of the primary wave's signal response. This adaptation subsequently enables the transfer of the findings obtained from synthetic signals to natural signals. The knowledge of the exact onset point of synthetic signals allows for determining the detection error precisely and paves the way for systematic error correction. The signal model

$$s : s[n, \theta) \in \mathbb{R},\ \theta \in \mathbb{R},\ n, N \in \mathbb{Z}_0^+,\ 0 \leq n \leq N-1 \tag{1}$$

of the discrete sampled synthetic signals is composed of the primary sinusoidal term T_1, the secondary sinusoidal term T_2, the primary damping term T_3, and the secondary damping term T_4

$$s[n, \theta) = \underbrace{[\sin(\omega\, n\, N_c)}_{T_1} - \underbrace{\frac{1}{\alpha} sin(\alpha\, \omega\, n\, N_c)]}_{T_2} \cdot \underbrace{\left(e^{-\frac{\beta\, n\, N_c}{N-1}}\right)}_{T_3} \cdot \underbrace{\left(1 - e^{-\frac{\gamma\, n\, N_c}{N-1}}\right)}_{T_4} \tag{2}$$

with the number of cycles $N_c \in \mathbb{Z}_0^+$ and $\omega = \frac{2\,\pi}{N-1}$. The number of samples $N = \left\lfloor N_c \frac{F_s}{F_1} \right\rfloor$ is related to the sampling frequency F_s in Hz and chosen such that N_c full wave cycles are obtained. The set of signal model parameters

$$\theta = \{F_1, \alpha, \beta, \gamma\} = \{F_1, 2, 0.5, 1.5\} \tag{3}$$

consists of the primary frequency F_1 in Hz, the ratio between primary and secondary frequency $\alpha = \frac{F_2}{F_1}$, the primary damping constant β, and the secondary damping constant γ. Unless otherwise specified, the values shown in (eq. 3) are constants concerning all computations.

A key prerequisite of the proposed onset point detection methods is the normalisation of the signal to the first local maximum's value $s|_{n_{\max,1}}$. Therefore, the normalised form of the signal model

$$\hat{s} = \frac{s}{s|_{n_{\max,1}}} \tag{4}$$

is used throughout this paper. A schematic representation of the signal model can be found in Fig. 2 (a), p. 8. See also function file[30] `/tools/tool_gen_signal.m`.

The detection parameter optimisation and the sensitivity analysis are based on clean test signals and test signals with additive i.i.d. noise to simulate natural signal behaviour. These signals are based on the zero-padded signal model

$$s_t[n] = \begin{cases} 0 & , 0 \leq n \leq L_{zp} - 1 \\ \hat{s}[n - L_z, \theta) & , L_z \leq n \leq L_z + N - 1 \end{cases} , \tag{5}$$

which is the basis of the test signal corrupted by Gaussian white noise (GWN)

$$x_t[n] = s_t[n] + \nu_s[n] \,. \tag{6}$$

Here, $L_z = \lfloor N_{c,z} \frac{F_s}{F_1} \rfloor$ is the zero-padding amount, $N_{c,z}$ is the number of cycles, and ν_s is the noise amplitude array scaled to a given SNR. The zero-padding helps to avoid unwanted boundary effects that may appear when computing the signal's envelope or applying sliding window detection. See also function file[30] `/tools/tool_gen_testsignal.m`. To simulate signals corrupted by noise with a given SNR, it is necessary to scale the noise amplitudes

$$\nu_s[n] = \nu[n] \cdot G_\nu \tag{7}$$

using the unscaled noise $\nu[n] = \mathrm{GWN}(\mu \approx 0, \sigma^2 \approx 1)$ and the noise gain

$$G_\nu = \sqrt{\frac{P_{\nu,\mathrm{SNR}}}{P_\nu}} \tag{8}$$

with

$$P_{\nu,\mathrm{SNR}} = \frac{P_s}{10^{\frac{\mathrm{SNR}}{10}}},\; P_\nu = \frac{1}{|w_m|} \sum_{(w_m)} \nu[n]^2,\; P_s = \frac{1}{|w_m|} \sum_{(w_m)} s_t[n]^2, \tag{9}$$

such that the given SNR is achieved within the power measuring window w_m : $L_z \leq n \leq L_z + L_m - 1$. The window length $L_m = \lfloor N_{c,m} \frac{F_s}{F_1} \rfloor$ is related to the signal model's primary frequency F_1 and the number of cycles $N_{c,m} = 1$ of the test signal. See also function file[30] `/tools/tool_scale_noise2snr.m`.

To be able to reproduce the analysis results, the unscaled noise data ν was generated in advance and saved to a noise standard file. The noise data is stored in the GNU Octave binary file `/results/noise_Nsmp8000_Nmc1000.oct` provided with the source code[30].

Natural signals. The natural signal data subjected to the analysis originate from laboratory experiments using the UPTM. The data sets containing the signal data (sequence of signals) are selected from four test series, each representing a different testing material. In test series 1 (cement paste tests), these

sequences consist of signals recorded every five minutes within the first 24 hours after adding water to the cement (288 signals). The signal sequences in the data sets of test series 5, 6 and 7 always consist of ten signals representing test repetitions related to a distinct device configuration.

To demonstrate the relevance of the proposed methods in terms of their practical applicability, they are tested against the signal data from the respective data sets. A list of the investigated data sets is available in Tab. 1, p. 9 and the corresponding schematic representation of the signal's structure is illustrated in Fig. 2 (b), p. 8.

Furthermore, detailed descriptions of the laboratory tests related to the signal data are available in a data descriptor[19] created by the author of this paper. Nevertheless, all relevant information regarding that signal data is also summarised in Tab. 2, p. 9.

Since the investigated signals are defined, the next step is to examine the applicability domains of the presented detection methods.

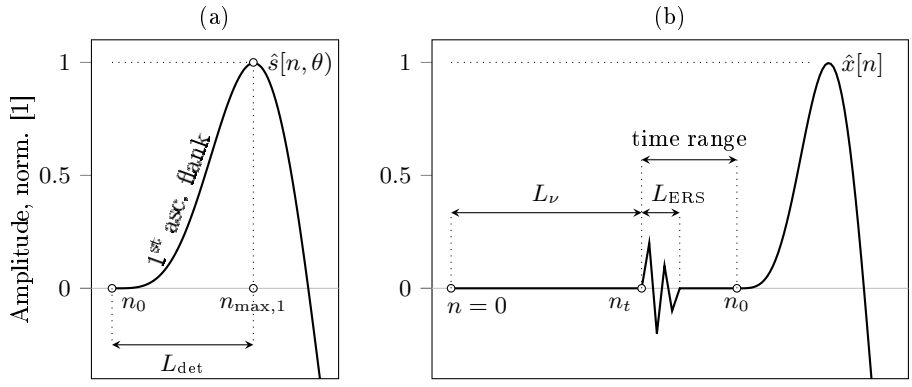

Figure 2: Synthetic and natural signal model. Schematic representation. **(a)** normalised synthetic signal (eq. 2, eq. 4). **(b)** normalised natural signal from UPTM tests. *Legend:* n_0 ... onset point index; n_t ... trigger point index ($t = 0$ s), L_ν ... pre-trigger section length (noise floor); L_{ERS} ... length of the electromagnetic response section (interference due to high-voltage pulse excitation).

2.2 Applicability domains

The methods presented and compared in this paper are primarily dedicated to the analysis of natural signal data gained by the ultrasonic pulse transmission method. Since these analysis methods used are not universally applicable to any signal data, the application domain for the signal model's primary signal frequency

$$F_1 : \mathrm{F_{low}} \leq F_1 \leq \mathrm{F_{upp}},\ 5 \leq F_1 \leq 150\ \mathrm{kHz} \tag{10}$$

and the noise expressed by the signal-to-noise ratio

$$\mathrm{SNR} : \mathrm{SNR_{low}} \leq \mathrm{SNR} \leq \mathrm{SNR_{upp}},\ 20 \leq \mathrm{SNR} \leq 63\ \mathrm{dB} \tag{11}$$

TS	Material	Data set file names	UMD [mm]
1	Cement paste	ts1_wc040_d25_4.oct[26]	25
1	Cement paste	ts1_wc040_d25_5.oct	25
1	Cement paste	ts1_wc040_d25_6.oct	25
1	Cement paste	ts1_wc040_d50_4.oct	50
1	Cement paste	ts1_wc040_d50_5.oct	50
1	Cement paste	ts1_wc040_d50_6.oct	50
1	Cement paste	ts1_wc040_d70_4.oct	70
1	Cement paste	ts1_wc040_d70_5.oct	70
1	Cement paste	ts1_wc040_d70_6.oct	70
5	Ambient air	ts5_d25_b⟨xx⟩_v800.oct[27]	25
5	Ambient air	ts5_d50_b⟨xx⟩_v800.oct	50
5	Ambient air	ts5_d70_b⟨xx⟩_v800.oct	70
5	Ambient air	ts5_d90_b⟨xx⟩_v800.oct	90
6*	Tap water	ts6_d25_b⟨xx⟩_v600.oct[28]	25
6*	Tap water	ts6_d25_b⟨xx⟩_v800.oct	25
6*	Tap water	ts6_d50_b⟨xx⟩_v600.oct	50
6*	Tap water	ts6_d50_b⟨xx⟩_v800.oct	50
6	Tap water	ts6_d70_b⟨xx⟩_v600.oct	70
6	Tap water	ts6_d70_b⟨xx⟩_v800.oct	70
6	Tap water	ts6_d90_b⟨xx⟩_v600_2.oct	90
6	Tap water	ts6_d90_b⟨xx⟩_v800_2.oct	90
7	Aluminium cylinder	ts7_d50_b⟨xx⟩_v400.oct[29]	50
7	Aluminium cylinder	ts7_d50_b⟨xx⟩_v600.oct	50
7	Aluminium cylinder	ts7_d50_b⟨xx⟩_v800.oct	50

Table 1: Selected datasets of test series 1, 5, 6 and 7. *Legend:* TS ... test series identifier; UMD ... ultrasonic measuring distance; ⟨xx⟩ = {16, 24, 32, 50} ... two-digit number representing the approximate length of the recorded block size in kilo-samples. *Note:* The datasets marked with an asterisk (test series 6, UMD 25 and 50 mm) are used for the signal model fitting procedure, but not for the further analysis, as the shape of these signals shows notable differences from the proposed signal model (see also Fig. 25 (g), (h), p. 61).

Name	**Value**	**Unit**	**Description**
V_p	800	V	pulse voltage (pulse generator)
w_p	2.5	μs	pulse width (pulse generator)
F_{res}	500	kHz	resonance frequency (piezoelectric transducer)
F_s	10	MHz	sampling frequency (oscilloscope)
R_v	16	bit	vertical resolution (oscilloscope)
N_μ	5	#	number samples, ensemble average (oscilloscope)

Table 2: Ultrasound testing device settings related to test series 1, 5, 6 and 7.

need to be defined. These two ranges define a two-dimensional parameter grid, with the grid points denoted as (F_1, SNR). This parameter grid represents the basis for the detection parameter optimisation and the sensitivity analysis described later.

Choice of parameter ranges. However, these parameter ranges are not chosen arbitrarily. As shown in the illustrations of the frequency range (see Fig. 23, p. 47) and SNR estimates (see Fig. 24, p. 47) based on hundreds of ultrasonic signals for different testing materials, the selected limits correspond to real-life conditions. Since a rough estimate of both parameters is sufficient for the following analyses, it is neither necessary nor proper to demand exact agreement at this point. Particular attention is paid to the lower limits $\mathrm{F_{low}}$ and $\mathrm{SNR_{low}}$, as remarkable detection errors are to be expected here and thus represent critical limits. The upper limits $\mathrm{F_{upp}}$ and $\mathrm{SNR_{upp}}$, on the other hand, solely restrict the investigated range.

Prerequisites and limitations. Almost all of the here-described detection methods rely on dual threshold detection to approximate a secant to the signal in the detection zone. Due to the method's design, additionally, the secant's gradient must be positive. Given that, the signal must exhibit strictly monotonically increasing amplitudes in that range. Without considering noise, this requirement also corresponds to the behavioural pattern observed in the ultrasonic signals examined here (see Fig. 25, p. 61). Concerning noise, it is necessary to relax the requirement regarding monotony. To be able to estimate the x-axis crossing of the secant, it is sufficient to require a non-zero secant gradient. However, the impact of noise, expressed by the SNR, still needs to be limited. The experience related to the analysis for this paper showed that the methods do not fail as long as the SNR is higher than 20 dB.

A key feature of the detection methods is to optimise the detection parameters according to the shape of natural signals concerning the detection zone. For the vast majority of signals analysed here, the above-described signal model fits well to natural signals in that range. As can be seen in Fig. 25 (g), (h), p. 61, this does not come without exceptions. In the analyses of this paper, natural signals that cannot be adequately described by the selected signal model $s[n, \theta)$ (eq. 2) are not further investigated (see also Tab. 1, p. 9).

Another key feature of the proposed methods is to use constant threshold values ($t \in \mathbb{R}^+,\ t < 1$) solely related to the signal model under consideration. Therefore, it is necessary to normalise the signal amplitudes to the first local maximum, who's location also determines the end of the detection zone. An alternative approach is to scale the threshold values accordingly. In both cases, it must be possible to detect the first local maximum and estimate the corresponding signal amplitude, which is a limitation of the method's applicability.

As mentioned earlier in the introduction, the proposed methods are based on a combination of well-established and straightforward approaches. These are described next.

2.3 Fundamental methods

All detection method presented in this paper rely on combinations of simple and well known techniques from classic signal analysis and statistics. These are subsequently listed, including a brief description of their use and parametrisation.

Threshold detection. This common detection method[15,16] is applied here in the form of dual threshold detection (two consecutive detection turns) and single threshold detection. It is performed either as a forward search or as a backwards search concerning the signal's sample index n. Due to its direct dependence on the signal amplitudes, interferences and noise are the leading cause of detection errors and false detections. A schematic representation of the detection problem can be found in Fig. 6, p. 21. See also function files[30] `/tools/tool_det_thfwd.m` and `/tools/tool_det_threv.m`.

Linear approximation. This method is used to estimate the secant to a discrete sampled function $f[n]$ (e.g., a signal). The two secant supports n_1 and n_2 are determined by dual threshold detection using the threshold values t_1, t_2. The function $g[n] = c_0 + c_1\, n$ with coefficients

$$c_0 = f|_{n_1} - c_1\, n_1, \text{ and } c_1 = \frac{f|_{n_2} - f|_{n_1}}{n_2 - n_1} \tag{12}$$

describes the secant line. See also function file[30] `/tools/tool_linapp.m`. The function returning the secant line's coefficients is subsequently briefly denoted by

$$\{c_0, c_1\} = \mathrm{LA2P}(n_1, n_2, f)\ . \tag{13}$$

Linear regression. The linear regression (least squares method) is also used to approximate the secant to a discrete sampled function $f[n]$ (e.g., a signal) but also during the detection parameter optimisation. That method delivers the coefficients

$$\{c_0, c_1\} = \underset{c_0, c_1}{\arg\min} \sum_{n=n_1}^{n_2} (f[n] - g[n])^2 \tag{14}$$

of the best-fitted linear secant function $g[n] = c_0 + c_1\, n$. Since that method is used extensively, it is subsequently denoted briefly with

$$\{c_0, c_1\} = \mathrm{REG1}(n_1, n_2, f)\ . \tag{15}$$

The realisation of that method, which employs the GNU Octave function `polyfit`, is available in the function file[30] `/tools/tool_linreg.m`.

Signal windowing. For a variety of purposes it is necessary to operate on certain portions of a signal (e.g., SNR estimates or optimisation intervals). For this purpose the following Dirichlet windows are used to refer to a certain portion

of the signal:

$$w_\nu[n] = 1 : 0 \leq n \leq n_t \text{ with } L_\nu = n_t + 1 \tag{16}$$

$$w_{\text{det}}[n] = 1 : n_0 \leq n \leq n_0 + L_{\text{det}} - 1 \text{ with } L_{\text{det}} = n_{\text{max},1} - n_0 + 1 \tag{17}$$

$$w_{\text{opt}}[n] = 1 : n_1 \leq n \leq n_1 + L_{\text{opt}} - 1 \text{ with } L_{\text{opt}} = \lfloor f_{L,\text{opt}} \cdot L_{\text{det}} \rfloor \tag{18}$$

$$w_{1,1}[n] = 1 : n_t + L_{\text{ERS}} \leq n \leq N - 1 \tag{19}$$

$$w_{1,2}[n] = 1 : n_{2,1} \leq n \leq n_{2,2} \text{ with} \tag{20}$$

$$n_{2,1} = \max\left(n_t + L_{\text{ERS}}, \left\lfloor \frac{n_0 + n_t + L_{\text{ERS}}}{2} \right\rfloor\right) \text{ and} \tag{21}$$

$$n_{2,2} = n_t + L_{\text{ERS}} + 3\,[n_0 - n_t - L_{\text{ERS}}] \tag{22}$$

$$w_2[n] = 1 : n_0 \leq n \leq n_0 + L_2 - 1 \text{ with } L_2 = 8\,(n_{\text{max},1} - n_0 + 1) \tag{23}$$

Thereby, n_0 is the onset point location, n_1 the support of the lower threshold t_1, n_2 the support of the upper threshold t_2, $f_{L,\text{opt}} = 0.4$ the preset optimisation interval length factor, and L_{ERS} the length of the electromagnetic response section (ERS, interference caused by pulse excitation). An illustration to the signal structure and the window placement can be found in Fig. 3, p. 12.

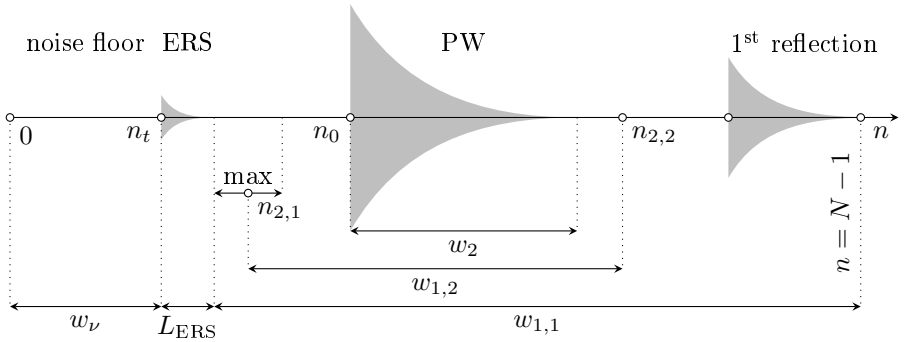

Figure 3: Schema of the structure of natural signals and window placement. *Legend:* PW ... primary wave; ERS ... electromagentic response section.

Sliding window double threshold detection. Inspired by the papers[13,18] of Barshan (2000) and Weihua et al. (2014), this method is used for comparison purposes. The method's core is the classification of signal amplitudes $x[n]$ using two coupled threshold values t_v and t_w, and a sliding Dirichlet window with length L_w and window shift index m. In this method, for each m, the ratio

$$r_{w,m} = \frac{1}{L_w} \sum_{n=m}^{m+L_w-1} (x[n] \geq t_v) \tag{24}$$

of signal amplitudes exceeding the first threshold value t_v is evaluated. Subsequently, the second threshold t_w is used to determine the smallest window shift

$$n_0 = m_{\text{det}} = \inf \arg_m (r_{w,m} \geq t_w) \tag{25}$$

for which the detection criterion $r_{w,m} \geq t_w$ is satisfied. That approach corresponds to the method "SW(A)" in the paper[18] of Barshan (see page 46) and is furthermore the basis of two comparison methods described later.

Monte Carlo simulation (MCS). MCSs are the very core of the sensitivity analysis and deliver the detection error data needed to describe the method's properties in terms of robustness to frequency and noise, and to measure the method's performance. Each simulation consists of a loop over N_{MC} simulation steps delivering the detection error $e_{\mathrm{det},i}$ for each step i, which are collected in the error data set X. In each MCS the following steps are carried out:

Require: p ... optimised detection parameters
function MCS(p)
  $\{s_t, n_0\} \leftarrow s_t[n, \theta)$ ▷ generate clean test signal (eq. 5)
  for $i = 1$ to N_{MC} **do**
    $\nu_{s,i} \leftarrow \nu_i \cdot G_{\nu,i}$ ▷ scale noise to given SNR (eq. 7, eq. 8)
    $x_{t,i} \leftarrow s_t + \nu_{s,i}$ ▷ add noise to signal (eq. 6)
    $\hat{n}_{0,i} \leftarrow \mathrm{DetectionMethod}(x_{t,i}, p)$ ▷ estimate onset point location
    $e_{\mathrm{det},i} \leftarrow \hat{n}_{0,i} - n_0$ ▷ compute detection error
    $X_i \leftarrow e_{\mathrm{det},i}$ ▷ collect detection errors
  end forreturn X_i
end function

The "DetectionMethod" refers to one of the onset point detection methods described below. See also function file[30] `/tools/tool_montecarlo_test.m`.

Parameter variations. The entire detection parameter optimisation is related to parameter variations. These are used to establish a set of property values for statistical assessments or error minimisation. The principle of these parameter variations is to vary one parameter p of a property function $f(p)$ within the discrete sampled interval $I_p : p_1 \leq p_k \leq p_K$ with K samples and to evaluate the property function at certain point, which yields the discrete-sampled property function

$$\hat{f}[k] = f(p_k, \{c_i\}) \tag{26}$$

with the set of constant function parameters $\{c_i\}$. It is worth noting that the property function's extreme values within the domain I_p are only approximations of the exact solution, as the domain is not smooth.

SNR estimates. The SNR is estimated along with the onset point detection concerning natural signals and allows for justifying whether detection takes place within the chosen limits (eq. 11) or not. The SNR estimates rely on the power estimates of the noise floor and the signal corrupted by noise concerning the power measuring windows w_ν (eq. 16), $w_{1,1}$ (eq. 19), $w_{1,2}$ (eq. 20), and w_2 (eq. 23). See also function file[30] `/tools/tool_est_snr.m`. Based on the power estimates

$$P_\nu = P_\nu(w_\nu) = \frac{1}{|w_\nu|} \sum_{(w_\nu)} x[n]^2,\ P_{x,1,1}(w_{1,1}),\ P_{x,1,2}(w_{1,2}) \text{ and} P_{x,2}(w_2), \tag{27}$$

the a priori SNR estimate (before onset point detection)

$$\text{SNR1} = 10\,\log_{10}\frac{P_{x,1,1} - P_\nu}{P_\nu} \text{ or } \text{SNR1} = 10\,\log_{10}\frac{P_{x,1,2} - P_\nu}{P_\nu} \tag{28}$$

and the a posteriori SNR estimate (after onset point detection)

$$\text{SNR2} = 10\,\log_{10}\frac{P_{x,2} - P_\nu}{P_\nu} \text{ follow.} \tag{29}$$

Finite Impulse Response (FIR) filter. A low-pass filter is applied to natural signals before estimating the frequency range and the primary wave's first local maximum. To narrow down the phase shift, the filter is always applied as zero-phase filter (cascaded filtering). See also function file[30] `/tools/tool_flt_fir.m`. The filter coefficients h are obtained from the Hanning window, where the filter order (number of taps)

$$N_{\text{taps}} = \left\lceil \frac{F_s}{F_{t,2} - F_{t,1}} \cdot \frac{A_{\text{dB}}}{22} \right\rceil = 36 \tag{30}$$

is chosen according to the Harris approximation[20] with $F_s = 10$ MHz, the upper pass-band limit $F_{t,1} = 500$ kHz, the lower stop-band limit $F_{t,2} = 780$ kHz, and the stop-band attenuation $A_{\text{dB}} = -22$ dB. An illustration of the filter's frequency response can be found in Fig. 4, p. 14.

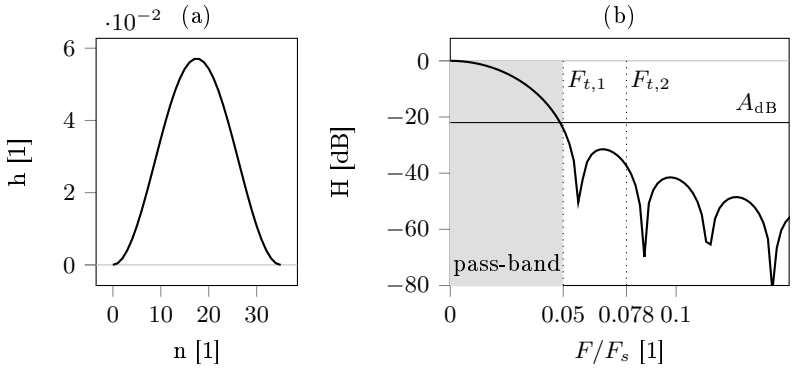

Figure 4: Finite impulse response low-pass filter. Number of fast Fourier transformation points $N_{\text{FFT}} = 1024$. **(a)** Hanning window h. **(b)** Frequency response H. *Legend:* F/F_s ... normalised frequency; $F_{t,1}$ ... upper pass-band limit; $F_{t,2}$ ... lower stop-band limit; A_{dB} ... stop-band attenuation.

Discrete Fourier Transformation (DFT). The frequency range of natural signals is estimated through a DFT-based measurement system within the window w_2 (eq. 23). First, the signal is filtered as described above to suppress frequencies above the piezoelectric transducer's resonance frequency $F_{\text{res}} = 500$ kHz. Second, the signal is zero-padded to ensure a minimum frequency resolution of 1 kHz (for $F_s = 10$ MHz, $N_{\text{FFT}} \geq 5000$). Due to the DFT's symmetry for real-valued signals, only the positive frequency range is considered (unilateral DFT). See also function file[30] `/tools/tool_est_dft.m`.

Frequency range estimates. The estimation of the frequency range of natural signals regards to the power spectral density (PSD) related to the above-described unilateral DFT. Furthermore, the frequency range of a signal is characterised here by the PSD's quantiles $q = (0.01, 0.05, 0.25, 0.50, 0.75, 0.95, 0.99)$. See also function file[30] `/tools/tool_est_fqband.m`.

Following the description of the fundamental methods, everything is in place to scrutinize the onset point detection methods.

2.4 Onset point detection and error correction methods

The proposed signal processing methods consist of a series of simple steps aimed at improving the estimation results of the onset point location using known techniques and simple calculations. The method's design is specifically targeted to minimise the influence of frequency and noise. The improvement in accuracy and precision of the presented methods are mainly owed to taking into account the signal's shape within the detection zone.

As already mentioned, two methods from the literature[15,18] are used for comparison purposes. To provide fair conditions, these are also adapted to the chosen signal model. Furthermore, two related methods including error correction are derived from these two comparison methods.

First, an overview of the methods is presented. Then, the approach for the maximum point detection and the detection parameter optimisation settings follow. Based on that, the approaches of the proposed detection methods, including the comparison methods, are detailed.

Overview of the detection and error correction methods.

LA represents the primary functional principle of almost all other methods proposed in this paper. It is a dual threshold detection method, where the two threshold supports provide the basis to approximate the signal in the detection zone with a secant line (linear approximation). The onset point is estimated by the secant line's x-axis crossing. The functional principle of this method is similar to the paper[15] of Piyush (2023), but comes with several adaptations as described below. See also function file[30] `/tools/tool_dtla.m`.

LAC emerges from method LA and supplements it with systematic error correction, which is the secondary functional principle of all methods proposed in this paper. The onset point estimate relies on the secant's x-axis crossing and a correction value, which is a function of the secant's gradient. See also function file[30] `/tools/tool_dtlac.m`.

LR is similar to method LA. The main difference is that the secant is a linear regression polynomial, where the two threshold supports determine the regression base interval. As with method LA, the onset point estimate is the secant line's x-axis crossing. See also function file[30] `/tools/tool_dtlr.m`.

LRC works analogously to method LAC and supplements it with systematic error correction. The only difference to method LAC is the definition of the secant line. See also function file[30] `/tools/tool_dtlrc.m`.

DH is a dual threshold detection method based on the signal's envelope, which relies on the Hilbert transformation[21]. The method is inspired by the paper[15] of Piyush et al. (2023), but comes with some adaptations concerning the signal's shape. As with method LA, the onset point estimate is the secant's x-axis crossing. See also function file[30] `/tools/tool_dh.m`.

DHC emerges from method DH and supplements it with systematic error correction, which is identical to the error correction approach of method LAC. See also function file[30] `/tools/tool_dhc.m`.

SW is a sliding window double-threshold detection method founded on the papers[13,18] of Barshan (2000) and Weihua et al. (2014), but as for method DH also adapted concerning the signal's shape. The most important enhancement is that the window length is determined automatically from the secant's gradient estimated analogous to method LAC. In contrast to all other methods described in this paper, the onset point estimate is related to the sliding window's shift index (lag) rather than the secant line's x-axis crossing. See also function file[30] `/tools/tool_dsw.m`.

SW emerges from method SW and supplements it with systematic error correction. Since the estimate for the secant gradient is already available through the automatic window length estimation, it is natural to employ the secant's gradient for systematic error correction analogous to method LAC. See also function file[30] `/tools/tool_dswc.m`.

Local maximum detection. As already explained in subsection 'Applicability domains', p. 8, the primary wave's first local maximum must be detectable in order to scale the signal or the threshold values, respectively. For this purpose, two different methods are employed.

The first method (DetInitMax) utilises the oscillation of the signal. First, the global minimum value $x_{\min}$ is determined within the interval $n_i \leq n \leq N-1$ (detection start index n_i). Second, a threshold detection with the threshold value $t = \frac{x_{\min}}{2}$ is carried out to determine the search limit $n_{\lim}$ located at the descending flank of the first negative lobe of the incoming primary wave. Finally, the local maximum's location $n_{\max,1}$ is found in the search interval $n_i \leq n \leq n_{\lim}$. The limiting factor for this method is that the minimum value of the first negative lobe need to be smaller than 0.5 times the global minimum value. See also function file[30] `/tools/tool_det_initmax.m`.

The second method (DetLocMax) is based on an iteration over the signal index n, beginning at the start index n_i. The signal index n is incremented until $c_{\lim}$ signal amplitudes are smaller than the continuously updated maximum $a = max(x[n], x[n-1])$, which is the loop's stop criterion. If the stop criterion is met, the first local maximum's location is determined by $n_{\max,1} = n - c_{\lim}$. The limiting factor of this method is the need to have at least a rough estimate for the counter limit $c_{\lim}$ related to the signal frequency. If $c_{\lim}$ is chosen too small, the noise may cause false detection. If $c_{\lim}$ is chosen too large, the iteration may run into the next positive lobe of the signal, and the stop criterion will either be met too late or not at all. In the best case, $c_{\lim} \approx \frac{F_s}{2\,F}$ is about half the wavelength. See also function file[30] `/tools/tool_det_localmax.m`.

Detection parameter optimisation settings. In the course of the detection parameter optimisation, several parameter variations are performed to find optimal values for the detection parameters (threshold values) for all onset point detection methods. To optimise the threshold values t_1, t_2 related to the methods LA, LAC, LR and LRC the lower boundary of the optimisation interval n_1 is varied within the interval

$$I_{n_1} : \left\lfloor \frac{L_{\text{det}}}{4} \right\rfloor \leq n_1 \leq \left\lfloor \frac{3\,L_{\text{det}}}{4} - \frac{L_{\text{opt}}}{2} \right\rfloor \text{ step } = 1 \tag{31}$$

with L_{det} (eq. 17), L_{opt} (eq. 18) and $f_{\text{L,opt}} = 0.4$. The optimisation is based on the normalised signal model $\hat{s}[n, \theta)$ (eq. 2, eq. 4) sampled with $F_s = 10{,}000$ kHz, $F_1 = 50$ Hz and $N_c = 3$ cycles. Concerning method DH the lower threshold value t_1 is varied within the interval

$$I_{t_1} : E(s_t)|_{n=L_z} \leq t_1 \leq 0.45, \text{ lin-spaced, M } = 100 \text{ items} \tag{32}$$

with the normalised envelope $E(s_t)$ (eq. 47) of the test signal $s_t[n, \theta)$ (eq. 5) and the length of the test signal's zero-padding section L_z. The test signal is sampled with $F_s = 10{,}000$ kHz, $F_1 = 50$ Hz, $N_c = 3$ cycles and $N_{c,z} = 1$.

In the course of optimisation related to the correction threshold value t_c related to the methods LAC, LRC, DHC and SWC, the signal models primary frequency F_1 is varied within the interval

$$I_{F_1} : 500 \leq F_1 \leq 15{,}000\,\text{Hz}, \text{ log-spaced, M } = 100 \text{ items.} \tag{33}$$

The test signal $s_t[n, \theta)$ (eq. 5) for the correction threshold optimisation is sampled with $F_s = 10{,}000$ kHz, $N_c = 3$ cycles and $N_{c,z} = 1$.

Detection and error correction approach. The detection and error correction methods rely on the two essential methods LA and LR. Both consist of dual threshold detection and estimate the primary wave's onset point using the x-axis crossing of the secant to the signal. They differ only in the method used to establish the secant function (see step **A2.1**, p. 18 and **A2.2**, p. 18). The method variants LAC and LRC supplement these with the error correction approach described in step **A3**, p. 18 and step **A7**, p. 19. A flowchart for these four methods can be found in Fig. 5, p. 20. The approach consists of the following constituent elements.

A1 Choice of a signal model $s[n, \theta)$ which is coherent to the natural signals x under investigation and estimate the signal model parameters $\hat{\theta}$ such that an optimal fit to the shape of the normalised signal $\hat{x}[n]$ is achieved within the detection range w_{det} (eq. 17). See also paragraph 'Parametrisation of the signal model', p. 27.

A2 Optimisation of the thresholds values t_1 and t_2 for dual threshold detection concerning the normalised signal model $\hat{s}[n, \theta)$ (eq. 2, eq. 4), $F_s = 10{,}000$ kHz and $N_c = 3$. In the course of the optimisation, the lower limit n_1 of the optimisation window w_{opt} (eq. 18) is varied within the interval I_{n1} (eq. 31) such that the square-sum of the residuals $\hat{s}[n, \theta) - g[n, c_i)$ approaches a minimum within the optimisation window (least squares method). To define the secant's discrete linear function $g[n, c_i)$, two options are considered:

A 2.1 Two-point form of $g[n, c_i)$ (eq. 12,eq. 13): The optimised threshold supports

$$n_{1,\mathrm{opt}} = \underset{n_1}{\arg\min} \sum_{n=n_1}^{n_1+L_{\mathrm{opt}}-1} (\hat{s}[n,\theta) - g[n, c_i))^2 \text{ and} \tag{34}$$

$$n_{2,\mathrm{opt}} = n_{1,\mathrm{opt}} + L_{\mathrm{opt}} - 1 \tag{35}$$

with $\{c_i\} = \mathrm{LA2P}(n_1, n_2, \hat{s})$ (eq. 12, eq. 13) deliver to the optimised threshold values

$$t_{1,\mathrm{opt}} = \hat{s}[n,\theta)|_{n_{1,\mathrm{opt}}} \text{ and } t_{2,\mathrm{opt}} = \hat{s}[n,\theta)|_{n_{2,\mathrm{opt}}} \tag{36}$$

of method LA and LAC.

A 2.2 Linear regression polynomial $g[n, c_i)$: The optimised threshold supports

$$n_{1,\mathrm{opt}} = \underset{n_1}{\arg\min} \sum_{n=n_1}^{n_1+L_{\mathrm{opt}}-1} (\hat{s}[n,\theta) - g[n, c_i))^2 \text{ and} \tag{37}$$

$$n_{2,\mathrm{opt}} = n_{1,\mathrm{opt}} + L_{\mathrm{opt}} - 1 \tag{38}$$

with $\{c_i\} = \mathrm{REG1}(n_1, n_2, \hat{s})$ (eq. 14, eq. 15) are the basis of the optimised secant polynomial coefficients $\{c_{i,\mathrm{opt}}\} = \mathrm{REG1}(n_{1,\mathrm{opt}}, n_{2,\mathrm{opt}}, \hat{s})$ and the optimised threshold values

$$t_{1,\mathrm{opt}} = g[n, c_{i,\mathrm{opt}})|_{n_{1,\mathrm{opt}}} \text{ and } t_{2,\mathrm{opt}} = g[n, c_{i,\mathrm{opt}})|_{n_{2,\mathrm{opt}}} \tag{39}$$

of method LR and LRC.

A3 Optimisation of the correction threshold value t_c concerning the test signal model $s_t[n,\theta)$ (eq. 5) with $F_s = 10$ MHz, $N_c = 3$ and $N_{c,\mathrm{zp}} = 1$. For that, the signal model's primary frequency F_1 is varied within the interval I_{F1} (eq. 33) subdivided into M steps. In each step m a dual threshold detection using the optimised threshold values $t_{1,\mathrm{opt}}$ and $t_{2,\mathrm{opt}}$ (eq. 36 or eq. 39) is performed. Furthermore, the secant's gradient c_{1m} (eq. 12 or eq. 14), the secant line's x-axis crossing n_{xm} (eq. 42), the correction value a_m (eq. 44) and the correction threshold t_{cm} (eq. 43) are evaluated. The variation results allow for describing the discrete relation $t_{c,\mathrm{cal}}[m]$ of the correction threshold t_c concerning the secant's gradient c_1. Finally, the discrete relation $t_{c,\mathrm{cal}}[m]$ is approximated by the first order polynomial

$$t_{c,\mathrm{app}}[n, t_c) = t_{c,0} + t_{c,1}\, n \tag{40}$$

with $\{t_{c,0}, t_{c,1}\} = \mathrm{REG1}(c_{11}, c_{1M}, t_{c,\mathrm{cal}})$ (eq. 14). The optimised correction threshold coefficients $t_{c,0}$ and $t_{c,1}$ of method LAC and LRC are related to the chosen secant approximation explained in **A 2.1**, p. 18 and **A 2.2**, p. 18. A by-product of the frequency variation is the discrete relation $k_{\mathrm{cal}}[m] = c_{1m}$ of the secant's gradient c_1 concerning the normalised frequency $f_1 = F_1/F_s$ approximated by the first order polynomial

$$k_{\mathrm{app}}(f_1, k) = k_0 + k_1\, f_1 \tag{41}$$

with $\{k_0, k_1\} = \mathrm{REG1}(f_1|_{m=1}, f_1|_{m=M}, k_{\mathrm{cal}})$ (eq. 14, eq. 15). The corresponding optimisation results are displayed in Fig. 10, p. 39.

A4 Detection of the first local maximum's location $n_{\max,1}$ and amplitude $x|_{n_{\max,1}}$ of the natural signal x corrupted by noise (see also paragraph 'Local maximum detection', p. 16). As a preconditioning measure, the signal is normalised to the maximum amplitude, which allows for using the same optimised threshold values regardless of the signal's actual amplitudes.

A5 Dual threshold detection using the optimised threshold values $t_{1,\mathrm{opt}}$ and $t_{2,\mathrm{opt}}$ (eq. 36 or eq. 39). In noisy environments, the low value of the lower threshold $t_{1,\mathrm{opt}}$ proves to be potentially unfavourable. To reduce the probability of false detection, a single threshold detection with the threshold t_0 ($\nu_{\max} < t_0 < 1$) is proposed here. Here, $\nu_{\max}$ is the maximum positive amplitude of the noise in the range between n_t and n_0. The resulting signal index n_i is subsequently used as the starting point for the dual threshold detection. A backwards search yields the support n_1, and a forward search yields the support n_2. An illustration to the detection scheme is shown in Fig. 6, p. 21.

A6 Estimation of the primary wave's onset point n_x. The secant line's x-axis crossing

$$n_x = n_1 - \frac{g|_{n_1}}{c_1} \tag{42}$$

delivers the first estimate for the onset point and the detection error

$$e_{\mathrm{det},x} = n_x - n_0 \tag{43}$$

of method LA and LR.

A7 Correction of the first onset point estimate n_x (eq. 42) using the correction threshold function $t_{c,\mathrm{app}}[n, t_{c,i})$ (eq. 40) from step **A3** and the secant's gradient c_1. The correction value

$$a = \frac{t_{c,\mathrm{app}}|_{c_1}}{c_1} = \frac{t_{c,0} + t_{c,1}\, c_1}{c_1} \tag{44}$$

allows to estimate the corrected onset point index

$$\hat{n}_0 = n_x - a \tag{45}$$

and the residual onset point detection error

$$e_{\mathrm{det},c} = \hat{n}_0 - n_0 \ . \tag{46}$$

of method LAC and LRC. An illustration to the error correction scheme can be found in Fig. 7, p. 21.

The comparison methods DH and DHC. The first comparison method, inspired by the paper[15] by Piyush et al. (2023), proposes a dual-threshold detection method with automatic error correction. That method operates on the envelope of the signal, rather than the signal itself, and furthermore suggests that the upper threshold value should be twice the lower threshold value. Since the paper does not provide precise details on how to estimate the envelope,

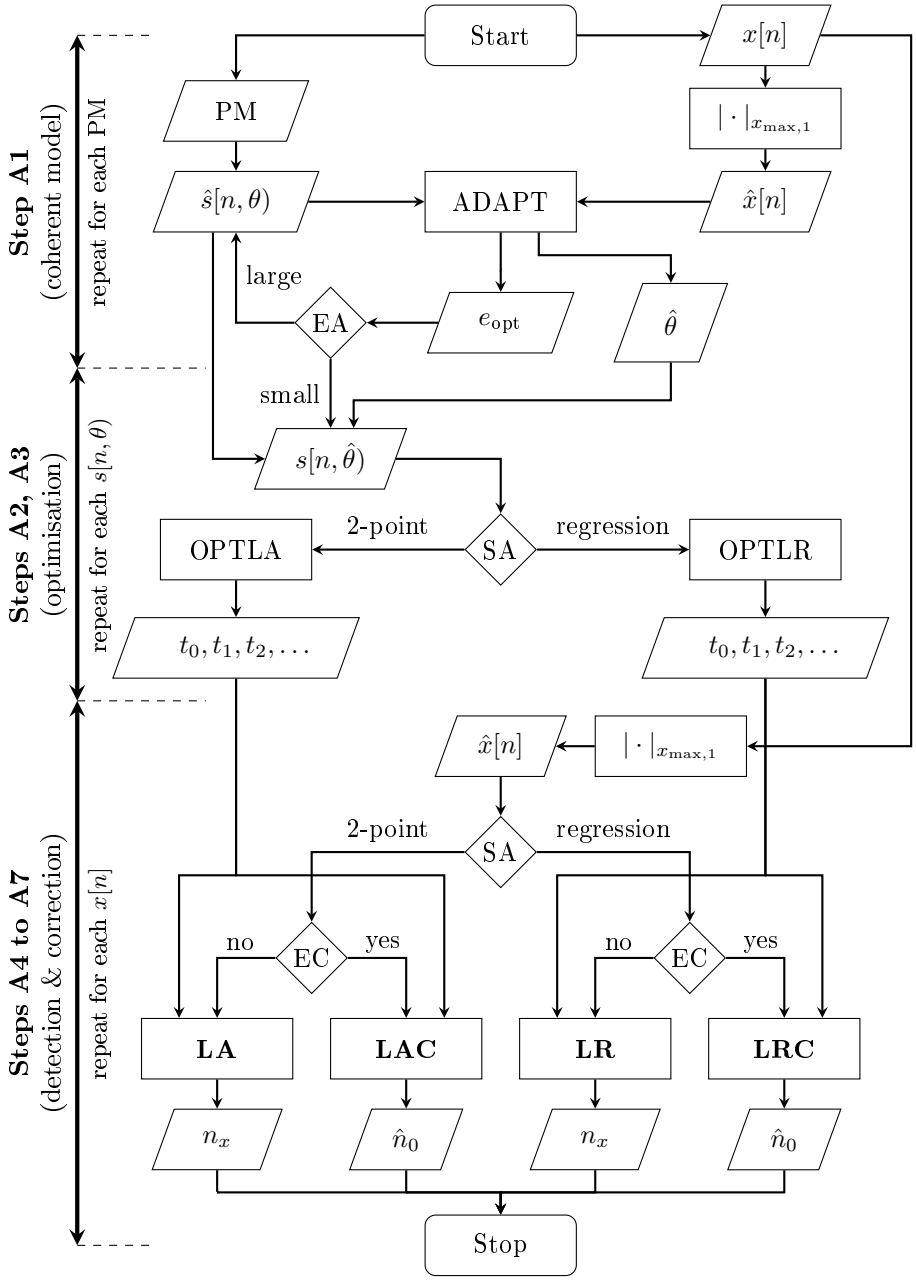

Figure 5: Method flowchart. *Legend:* PM ... physical model; EA ... error assessment; SA ... secant approximation mode; OPTLA ... threshold value optimisation, parametrise secant using the 2-point form of a line; OPTLR ... threshold value optimisation, parametrise secant using a linear regression; t_i ... optimised threshold values; EC ... error correction mode; , n_x, $\hat{n}_{0,i}$ ... estimate onset point location.

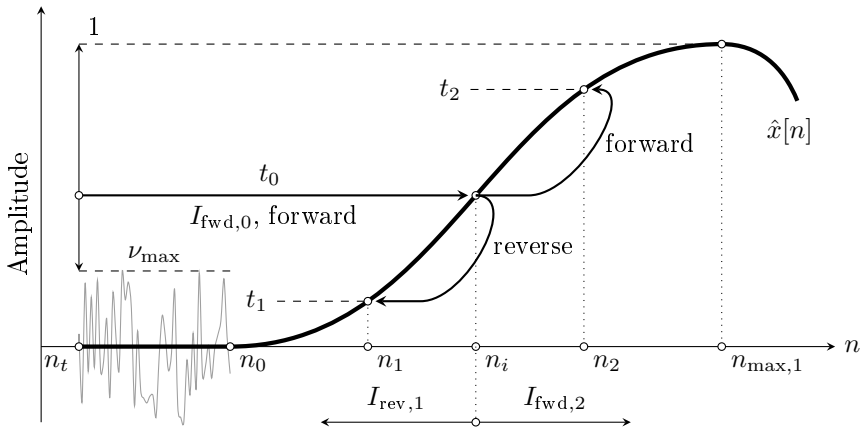

Figure 6: Dual threshold detection schema. Initial threshold detection and dual threshold detection. *Legend:* $\hat{x}[n]$ ... normalised signal corrupted by noise; t_0 ... initial threshold; t_1 ... lower threshold; t_2 ... upper threshold; n_i ... initial threshold support; n_1 ... lower threshold support; n_2 ... upper threshold support; $n_{\max,1}$ ... first local maximum point; $\nu_{\max}$ ... the noise floor's maximum amplitude; $I_{\mathrm{fwd},0}$ ... initial forward search interval; $I_{\mathrm{rev},1}$ ... lower reverse search interval; $I_{\mathrm{fwd},2}$ ... upper forward search interval.

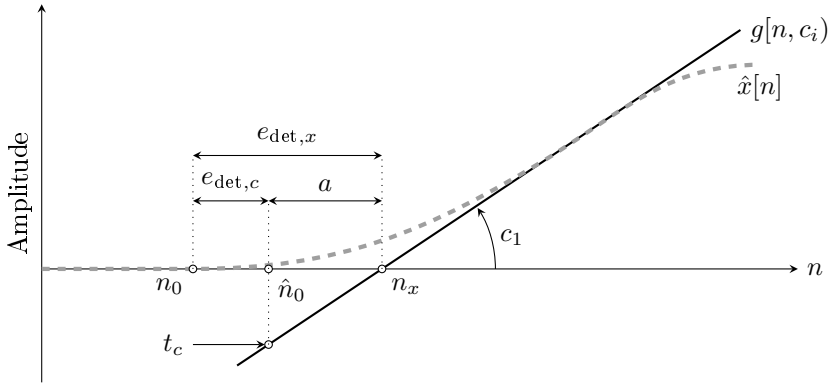

Figure 7: Onset point correction schema. *Legend:* $\hat{x}[n]$ ... normalised signal corrupted by noise; $g[n, c_i)$ ... secant function; c_1 ... secant gradient n_0 ... exact onset point index; $\hat{n}_0$ ... corrected onset point index; n_x ... secant x-axis crossing, first onset point estimate; t_c ... correction threshold (function of c_1); a ... correction value; $e_{\mathrm{det},x}$ ... residual error, first onset point estimate; $e_{\mathrm{det},c}$ ... residual error, corrected onset point.

the envelope based on the Hilbert transformer[21] is used here. However, the suggested proportion between the threshold values remains. Furthermore, the Hilbert transform is realised by the GNU Octave function `hilbert`, which relies on the fast Fourier transformation.

The below-described procedural steps **B1** to **B3** refer to the detection parameter optimisation concerning synthetic signals, and **B4** to **B8** describe the onset point detection procedure as applied to natural signals.

B1 Choice of a coherent signal model $s[n, \theta)$. See **A1**, p. 17.

B2 Optimisation of the thresholds t_1 and t_2 for dual threshold detection concerning the normalised envelope

$$E(s_t) = \frac{||s_t + j \cdot \mathrm{H}(s_t)||}{max(||s_t + j \cdot \mathrm{H}(s_t)||)} \tag{47}$$

with the imaginary unit j and the Hilbert transformer H. The search interval for the envelope's maximum value is restricted to the first cycle of the test signal s_t (eq. 5) sampled with $F_s = 10\,\mathrm{MHz}$, $N_c = 3$ and $N_{c,\mathrm{zp}} = 1$. The optimisation relies on the variation of the lower threshold t_1 within the variation interval I_{t1} (eq. 32) subdivided into M steps. In each step m a dual threshold detection with the thresholds t_{1m} and $t_{2m} = 2\,t_{1m}$ is performed. Furthermore, the respective threshold supports n_{1m} and n_{2m}, and the envelope's secant function $g[n, c_{im})$ (eq. 12) are evaluated. The optimal lower threshold $t_{1,\mathrm{opt}}$ is chosen such that the square-sum of the residual approaches a minimum within the error measuring window $n_{1m} \leq n \leq n_{2m}$ (least-squares method). This yields the optimised threshold values

$$t_{1,\mathrm{opt}} = \underset{t_1}{\operatorname{argmin}} \underset{m}{} \sum_{n=n_{1m}}^{n_{2m}} (E(s_t) - g[n, c_{im}))^2 \text{ and} \tag{48}$$

$$t_{2,\mathrm{opt}} = 2\,t_{1,\mathrm{opt}} \tag{49}$$

with $\{c_{im}\} = \mathrm{LA2P}(n_{1m}, n_{2m}, E(s_t))$ (eq. 12, eq. 13).

B3 Optimisation of the correction threshold t_c concerning $E(s_t)$ but otherwise analogous to **A3**, p. 18. The corresponding optimisation results can be found in Fig. 11, p. 40.

B4 Maximum point detection and amplitude normalisation as described in **A4**, p. 19 deliver the first local maximum's location $n_{\mathrm{max},1}$ and the normalised signal $\hat{x}$.

B5 Localisation of the first x-axis crossing n_{xc} behind the first local maximum point using $n_{\mathrm{max},1}$ as a starting point for a forward search. To increase the accuracy of the detection results for coarsely sampled signals, a linear interpolation between the samples around the x-axis crossing yields $\hat{n}_{xc}$.

B6 Estimation of the natural signal's normalised envelope

$$E(\hat{x}) = \frac{||\hat{x} + j \cdot \mathrm{H}(\hat{x})||}{max(||\hat{x} + j \cdot \mathrm{H}(\hat{x})||)}\,. \tag{50}$$

B7 Dual threshold detection using the optimised threshold values $t_{1,\mathrm{opt}}$, $t_{2,\mathrm{opt}}$ and $E(\hat{x})$. The search interval of the maximum value is restricted to $n_t \leq n \leq \hat{n}_{xc}$. See also **A5**, p. 19.

B8 Estimation of the secant line's x-axis crossing delivers the estimate onset point location n_x (eq. 42) and the detection error $e_{\mathrm{det},x}$ (eq. 43) of method DH. See also **A6**, p. 19.

B9 Correction of the onset point estimate n_x using the correction threshold t_c yields the estimate onset point index $\hat{n}_0$ (eq. 45) and the residual detection error $e_{\mathrm{det},c}$ (eq. 46) of method DHC. See also **A7**, p. 19.

The comparison methods SW and SWC. The second comparison method[18] is the sliding window double-threshold detection (see also paragraph 'Sliding window double threshold detection', p. 12). That method is adapted here concerning the signal model $s[n,\theta)$ (eq. 2) and supplies the adapted method SW. The adaptations essentially consist of the automated determination of the sliding window's length and the optimisation of the threshold values concerning the signal model's shape. The method SWC is a derivative of the adapted method SW and supplements it with systematic error correction.

The below-described procedural steps **C1** to **C4** refer to the detection parameter optimisation concerning synthetic signals, and **C5** to **C8** describe the onset point detection procedure as applied to natural signals.

C1 Choice of a coherent signal model $s[n,\theta)$. See **A1**, p. 17.

C2 Optimisation of the threshold t_w concerning the normalised signal model $\hat{s}[n,\theta)$ (eq. 4), $F_s = 10$ MHz and $N_c = 3$. First, the threshold t_v is set to 0.5 and the sliding window's length L_w is set to L_{det} (eq. 17). These presets allow for estimating the threshold value

$$t_w \approx \frac{\sum_{n=n_0}^{n_{\mathrm{max},1}} \hat{s}[n,\theta) \geq t_v}{L_w} \tag{51}$$

as a function of the signal model.

C3 Optimisation of the threshold values t_1 and t_2 as described in **A2**, p. 17 and **A2.1**, p. 18. The corresponding optimisation results are displayed in Fig. 11, p. 40.

C4 Optimisation of the correction threshold t_c as described in **A3**, p. 18.

C5 Maximum point detection and amplitude normalisation as described in **A4**, p. 19 deliver the first local maximum's location $n_{\mathrm{max},1}$ and the normalised signal $\hat{x}$.

C6 Automated estimation of the sliding window's length L_w by performing a dual threshold detection with the optimised thresholds $t_{1,\mathrm{opt}}$ and $t_{2,\mathrm{opt}}$ (eq. 36) from step **C3**, p. 23. The threshold detection is necessary to evaluate the distance $L_{\mathrm{opt}} = n_2 - n_1 + 1$ between the two threshold supports n_1 and n_2, which allows for estimating the length of the sliding window

$$L_w = \left\lceil \frac{L_{\mathrm{opt}}}{f_{L,\mathrm{opt}}} \right\rceil \approx L_{\mathrm{det}},\ L_w \geq 5 \text{ samples}, . \tag{52}$$

Thus, L_w is an approximation of the detection window length L_{det} used during the optimisation in step **C2**, p. 23.

C7 Sliding of the previously shaped detection window along the signal index until the detection criterion (eq. 25) is met. See also paragraph 'Sliding window double threshold detection', p. 12. The window shift m_{det} provides the onset point index estimate n_x of method SW.

C8 Correction of the onset point estimate n_x using the correction threshold t_c delivers the estimate onset point index $\hat{n}_0$ (eq. 45) and the residual detection error $e_{\text{det},c}$ (eq. 46) of method SWC. See also **A7**, p. 19.

Since the detection methods are defined, the next step is to define the metrics needed to quantify the method's properties.

2.5 Performance standards and metrics

In this section, the performance standards and metrics are defined. These are used to measure the detection error and to assess the method's accuracy, precision, complexity, robustness to frequency and noise, and performance.

In the following explanations, the detection error e_{det} is always calculated in samples. In some situation, time provides a better impression about the error magnitude. Thus, the error is scaled by the actual sampling frequency F_s and the power 10^6 to micro-seconds μs (e.g., Fig. 18, p. 45).

Curve fitting error. To estimate the onset point detection error, knowing the true location of the onset point is mandatory. In the coherent literature[18], curve fitting is characterised as the most accurate estimation method. Therefore, the proposed signal model $s[n\theta)$ (eq. 2) is fitted in the detection zone (error measuring window) to natural signals taken from the data sets described in Tab. 1, p. 9. The fitting error is measured by the sum of the weighted mean-square errors (error score)

$$e_f = e_1\,\varphi_1 + e_2\,\varphi_2 \text{ with } \varphi_1 = \frac{2}{3}, \varphi_2 = \frac{1}{3} \text{ and} \tag{53}$$

$$e_1 = \frac{1}{n_c - n_1 + 1} \sum_{n_1}^{n_c} (\hat{x}[n] - \hat{s}[n - n_1, \theta))^2 \tag{54}$$

$$e_2 = \frac{1}{n_2 - n_c} \sum_{n_c+1}^{n_3} (\hat{x}[n] - \hat{s}[n - n_1, \theta))^2 \tag{55}$$

concerning the first and the second half of the error measuring window w_m : $n_1 \leq n \leq n_2$ with the centre index $n_c = \lceil \frac{n_2 - n_1 + 1}{2} \rceil$. The unequal choice of the weights φ_1 and φ_2 additionally enforces a better fit in the first half of w_m. In the below-described curve fitting procedure (see also paragraph 'Parametrisation of the signal model', p. 27), the fitting error is minimised iteratively by varying the index n_2 and the signal model parameters θ. A by-product of the error minimisation are the estimates for the onset point index $\hat{n}_{0,f} = n_1$, the index of the first local maximum $n_{\max,1} = n_2$, and the signal model parameters $\hat{\theta}$.

Detection error concerning synthetic signals. For synthetic signals, the exact location of the onset point n_0 is known. The detection error $e_{\mathrm{det},x}$ related to the methods without error correction (LA, LR, DH, SW) is estimated by eq. 43. The detection error $e_{\mathrm{det},c}$ related to the methods with error correction (LAC, LRC, DHC, SWC) is estimated by eq. 46.

Detection error concerning natural signals. For natural signals, the onset point location estimates from the curve fitting procedure serve as an approximation for the exact but unknown onset point location. Furthermore, the least-squares method employed for curve fitting is independent of the other detection methods and the onset point estimates are not biased by manual interventions. Therefore, these estimates are independent and objective and provide a proper reference to assess the onset point detection errors

$$e_{\mathrm{det},f,x} = \hat{n}_{0,f} - n_x \text{ and} \tag{56}$$

$$e_{\mathrm{det},f,c} = \hat{n}_{0,f} - \hat{n}_0 \,, \tag{57}$$

which result from the difference between the curve fitting solution $\hat{n}_{0,f}$ and the algorithmically calculated estimates n_x (LA, LR, DH, SW) or $\hat{n}_0$ (LAC, LRC, DHC, SWC).

Normalisation for comparison purposes. In this paper, the method' properties are described comparatively rather than by absolute numbers. Thus, the method's property metrics M_i are quantified by the normalised metrics score

$$\overline{M}_i = \frac{M_i - \min(M_i)}{\max(M_i) - \min(M_i)} \,. \tag{58}$$

For some properties (e.g., sensitivity, accuracy, precision), it makes sense to invert the method metrics (e.g., little sensitivity means strong robustness). The normalised and inverted metric score is quantified by

$$\overline{M}_i^{(-1)} = 1 - \overline{M}_i \,. \tag{59}$$

Sensitivity and robustness. The sensitivity is a method metric describing the detection error cumulatively based on a set X_j consisting of K_j detection errors $e_{\mathrm{det},k}$ (e.g., eq. 43, eq. 46, eq. 56, eq. 57). The sensitivity is quantified by

$$S_j = \frac{1}{K_j} \sum_{k=1}^{K_j} (e_{\mathrm{det},k} - e_{\mathrm{exp}})^2 \tag{60}$$

concerning the expected error $e_{\mathrm{exp}} = 0$. When combining J sets, these are simply accumulated with $\overline{X} = \bigcup_{j=1}^{J} X_j$ before calculating the sensitivity.

The Robustness is the opposite of the sensitivity because it takes high values when the sensitivity is low. It is therefore measured by the normalised and inverted metric score (eq. 58, eq. 59)

$$R = \overline{S}^{(-1)} \,. \tag{61}$$

Complexity. One common method[22] to estimate the numerical complexity of an algorithm is measuring the time span elapsed to calculate the result. That time span is related to the amount of signal data to process and the number of numerical operations needed to compile the result. To cover the full range of varying frequencies (eq. 10) and SNRs (eq. 11), the time measurements T_{ij} are carried out during the two-dimensional parameter variation concerning frequency and SNR (see also paragraph 'Sensitivity analysis', p. 31). The complexity is defined by the cumulative metric

$$C = \frac{1}{N_{\text{var}}^2} \sum_{i=1}^{N_{\text{var}}} \sum_{j=1}^{N_{\text{var}}} T_{ij} \,. \tag{62}$$

It is worth noting that the computational effort for setting up the signal data is the same for all methods and, therefore, not taken into account. To avoid side effects related to the kernel's background processes, the MCSs were carried out on two isolated cores of an eight-core processor (11th Gen Intel(R) Core(TM) i7-1185G7 @ 3.00GHz).

Accuracy and precision. The method's accuracy and precision estimates are based on the detection error set X from a MCS with N_{MC} turns. The method's accuracy A is related to the mean value

$$\mu = \frac{1}{N_{\text{MC}}} \sum_{i=1}^{N_{\text{MC}}} e_{\text{det},i} \sim A \tag{63}$$

and the precision P is related to the empirical standard deviation

$$\sigma = \sqrt{\frac{1}{N_{\text{MC}} - 1} \sum_{i=1}^{N_{\text{MC}}} \left(e_{\text{det},i} - \mu\right)^2} \sim P \,. \tag{64}$$

In addition, a χ^2-test is carried out to justify whether the method's detection error distributions approximately correspond to the normal distribution and can be expressed meaningfully by the normal deviation's parameters μ and σ.

χ^2 homogeneity test. This distribution test[23] serves to check the homogeneity of the method's detection error distribution (observation p_o, sample X_o, $N_o = N_{\text{MC}} = 1000$) against the normal distribution (expectation p_e, sample X_e, $N_e = 10000000$). If the hypothesis $H_0 : p_o = p_e$ is accepted, the observed distribution belongs to the normal distribution and its parameters mean value μ and standard deviation σ are valid means of describing the error distribution (two parameters, $l = 2$). See also function file[30] `/tools/tool_chi2_distrtest.m`.

- First, a comparison sample $X_e = N(\mu_{x_o}, \sigma_{x_o})$ representing the normal distribution parametrised with the observation's μ_{x_o} and σ_{x_o}, is generated. See also GNU Octave function `normrnd` (Ziggurat method[24]).
- Second, the number of histogram classes (bins) is determined using the Freedman-Diaconis rule[25]

$$N_{\text{bin}} = \left\lceil \frac{\max(X_o) - \min(X_o)}{\sqrt[3]{2\,\left[q_{0.75}(X_o) - q_{0.25}(X_o)\right]}} \right\rceil \,, \tag{65}$$

where $q_{0.25}$ and $q_{0.75}$ are the lower and upper quartile of the observation. From that, the χ^2 distribution's degrees of freedom (number of classes) $m = N_{\text{bin}} - l - 1$ can be computed. The class limits c can then obtained from the equally spaced interval $\min(x_o) \leq c \leq \max(x_o)$ consisting of m items.

- Third, χ^2 and χ^2_{crit} are evaluated using the significance level $\alpha = 0.95$. See also GNU Octave functions `chisquare_test_homogeneity` and `chi2inv` (statistics package).
- If $\chi^2 < \chi^2_{\text{crit}}$ or $\chi^2/\chi^2_{\text{crit}} < 1$, the hypothesis is accepted and the compared distributions are homogeneous.

Performance score. That score is a useful tool to combine several method metrics in one number. The methods performance score is quantified by the composite metrics score

$$S = \frac{1}{N_i} \sum_{i=1}^{N_i} \overline{M}_i^{(-1)} \tag{66}$$

based on the normalised and inverted method metrics $\overline{M}_i^{(-1)}$ (eq. 59). The method metrics M_i are: complexity C (eq. 62), accuracy A (eq. 63) and the precision P (eq. 64), thus $N_i = 3$. See also function file[30] `/tools/tool_comp_perf.m`.

Now, everything is in place to apply the methods to synthetic and natural signal data using the above-described detection methods and metrics.

2.6 Analysis procedures

Based on the method's definitions and the metrics defined before, it is now to prove the method's functionality using the analysis procedures described below. These are targeted to show that the proposed signal model fits natural signals, to optimise the detection parameters, to examine the method's detection error properties concerning the signal model and to demonstrate that the methods apply not only to single natural signals, but to entire sequences of natural signals from UPTM tests. Based on the synthetic and natural signal data described in subsection 'Materials', p. 6, the below-described analyses are carried out.

Parametrisation of the signal model. To estimate the onset point detection error, knowing the actual location of the onset point is mandatory. In this procedure, the parameters of the signal model $s[n, \theta)$ (eq. 4) are chosen such that the signal model's shape fits ultrasound signals from selected data sets of four test series representing four different testing materials (cement paste, ambient air, tap water, and aluminium cylinder). A by-product of the below-described parametrisation procedure are the estimates for the onset point $n_{0,f}$ and the location of the first local maximum $n_{\max,1,f}$. The parametrisation of the signal model is a semi-automated procedure consisting of the following steps:

1. Visual inspection of the primary wave's signal response $x[n]$ and manual selection of a signal index n_s, which is to be located directly behind the maximum of the first lobe of the incoming primary wave.

2. Signal preconditioning by removing the constant bias from the signal amplitudes. As an additional stabilisation measure, the signal amplitudes between the signal start index and the end of the electromagnetic response section are set to zero, which yields the preconditioned signal x_d.

3. Localisation of the first x-axis crossing n_{xc} behind the first local maximum point using n_s as a starting point for a forward search ($x_d[n_s] > 0$) or backward search ($x_d[n_s] < 0$). Linear interpolation between the samples around the x-axis crossing yields $\hat{n}_{xc}$ and increases the accuracy of the detection results for coarsely sampled signals.

4. Localisation of the first local maximum of x_d yields $n_{\max,1}$. To reduce the impact of noise, a local polynomial of 2^{nd} order is fitted to the signal in the area $n_{\max,1} - L_{\text{fit}} \leq n \leq n_{\max,1} + L_{\text{fit}} - 1$ around the maximum point using the least-squares method.

$$L_{\text{fit}} = \left\lceil \frac{\hat{n}_{xc} - n_{\max,1} + 1}{2} \right\rceil \text{ samples} \tag{67}$$

   The polynomial fitting is only applied if $L_{\text{fit}} \geq 10$ samples. Therefore, the maximum point is either the already detected maximum or the maximum of the local regression polynomial.

5. Normalisation of the signal amplitudes.

$$\hat{x}_d = \frac{x_d}{x|_{n_{\max,1}}} \tag{68}$$

6. Estimation of an appropriate initial value $F_{1,0}$ of the signal model's primary frequency F_1.

$$F_{1,0} = F_s \frac{3}{4} \frac{r_{\max,1}}{L_0} \text{ with} \tag{69}$$

$$L_0 = \max(\hat{n}_{xc} - n_{\max,1} + 1, 3) \text{ samples}, \tag{70}$$

$$r_{\max,1} = \frac{k_{\max,1}}{K} \text{ and } k_{\max,1} = \arg\max \hat{s}[k, \theta_0) \ . \tag{71}$$

   The normalised reference signal $\hat{s}[k, \theta_0)$ (eq. 4) is only used to determine the relative location $r_{\max,1}$ of the maximum point concerning the chosen initial signal model parameters θ_0 ($F_{1,0}$, α_0, β_0, γ_0). K is the number of samples of one complete cycle related to the sampling frequency $F_s = 10^8$ Hz. See also function file[30] `/tools/tool_cyrat_sigmod.m`.

7. Perform a check whether the estimated initial onset point is located behind the signal's trigger point n_t. If the condition

$$n_t < n_{\max,1} - r_{\max,1} \frac{F_s}{F_1} \tag{72}$$

   is not met, the detection limit is reached, and the fitting procedure is aborted.

8. Parametrisation of the signal model using the least-squares method. The procedure consists of two nested loop cycles. Since the previously estimated maximum location is not necessarily the optimal solution, the index of the maximum point is varied in the outer loop using the variation interval $n_{\max,1} \pm 1$. In the inner loop, the signal model parameters F_1, α, β and γ are chosen such that the curve fitting error e_f (eq. 54) approaches a minimum. The variation interval for F_1 is $F_{1,0} \cdot f_1 \leq F_{1,k} \leq F_{1,0} \cdot f_2$ with $1 \leq k \leq K = 30$, which applies to the parameters α, β and γ likewise. The range factors f_1, f_2 and the initial values α_0, β_0 and γ_0 are tabulated in Tab. 3, p. 30. Shifting the variation interval up to four times is a measure to avoid solutions at the limits of the variation interval, which means that the global minimum was not found. If the solution remains at one of the interval limits after being shifted four times, it is nevertheless accepted. Additionally, interpolating the preconditioned natural signal $\hat{x}_d$ linearly by a factor of 10 helps to increase the accuracy of the signal model parameter and onset point estimates. ($\hat{x}_d[n] \mapsto y[m]$). The parametrisation procedure consists of the following steps:

   (a) outer loop:

$$\{m_{0,f}, m_{\max,1,f}, \theta_{opt}\} = \arg\min_j e_f(m_{\max,1,j}, F_{1,0}, \alpha_0, \beta_0, \gamma_0) \quad (73)$$

   (b) inner loop:

$$F_{1,opt} = \underset{F_1}{\operatorname{argmin}} \underset{k}{} e_f(m_{\max,1,j}, F_{1,k}, \alpha_0, \beta_0, \gamma_0) \quad \text{step 1} \quad (74)$$

$$\alpha_{opt} = \underset{\alpha}{\operatorname{argmin}} \underset{k}{} e_f(m_{\max,1,j}, F_{1,opt}, \alpha_k, \beta_0, \gamma_0) \quad \text{step 2} \quad (75)$$

$$\beta_{opt} = \underset{\beta}{\operatorname{argmin}} \underset{k}{} e_f(m_{\max,1,j}, F_{1,opt}, \alpha_{opt}, \beta_k, \gamma_0) \quad \text{step 3} \quad (76)$$

$$\gamma_{opt} = \underset{\gamma}{\operatorname{argmin}} \underset{k}{} e_f(m_{\max,1,j}, F_{1,opt}, \alpha_{opt}, \beta_{opt}, \gamma_k) \quad \text{step 4} \quad (77)$$

   At the end of the parametrisation procedure, the index of the optimisation results $m_{0,f}$ and $m_{\max,1,f}$ is transformed back to the signal index n, which yields $n_{0,f}$ and $n_{\max,1,f}$. If the residual curve fitting error exceeds the predefined value (see Tab. 3, p. 30), the detection limit is reached. See also function file[30] `/tools/tool_fit_sigmod.m`.

The signal model parameter and fitting error statistics can be found in Fig. 8, p. 37 and Tab. 4, p. 36. Additionally, exemplary curve fitting results for selected signals are displayed in Fig. 25, p. 61. See also function files[30] `algo_sigfit.m` and `algo_part_1.m`.

The impact of deviations in the signal model parameters. In addition to the signal model parametrisation, the impact of deviations in the signal model parameters is of interest to gain an impression of which signal model parameters need to be optimised with care and which parameters play a subordinate role. This impact assessment is carried out for each testing material (each test series) separately using the signal model parameter's median values from the curve fitting statistics (see Tab. 4, p. 36). These are the centre values of the parameter

Signal model parameters				
Name		α_0	β_0	γ_0
Initial state		2	0.5	1.5
Parameter variation settings				
TID	Material	f_1	f_2	$e_{f,\max}$
1	cement paste	0.25	1.50	0.001
2	ambient air	0.75	1.25	0.001
3	tap water	0.75	1.25	0.009
4	aluminium cylinder	0.75	1.25	0.001

Table 3: Curve fitting settings. Initial signal model parameter, variation range factors and the maximum fitting error. *Legend:* TID ... test series identifier; f_1, f_2 ... variation range factors; $e_{f,\max}$ ... upper limit of the acceptable curve fitting error. *Note:* $e_{f,\max}$ for test series 6 (tap water) is chosen much higher to demonstrate that the signal model does not fit all signals.

variation ranges $\alpha_0 \pm 20\,\%$, $\beta_0 \pm 20\,\%$, $\gamma_0 \pm 20\,\%$ subdivided into $K = 20$ variation steps. The impact of deviations in the signal model parameters is measured by the following procedure:

1. Reference signal setup: $s_r[n] = \hat{s}[n, \theta_r)$ (eq. 2, eq. 4) with $F_s = 100{,}000$ Hz, $N_c = 1$, $F_1 = 1$ Hz, $\theta_0 = \{F_1, \alpha_0, \beta_0, \gamma_0\}$ and the corresponding error measuring window $0 \leq n \leq n_{\max,1,r}$.

2. Looping through the parameter range related to α to evaluate the mean-square error $e_{\alpha,k}$ between the current test signal $s_k[n]$ and the reference signal $s_r[n]$ for each step k.

   (a) Test signal setup: $s_k[n] = \hat{s}[n, \theta_k)$ (eq. 2, eq. 4) with $\theta_k = \{F_1, \alpha_k, \beta_0, \gamma_0\}$, $F_s = 100{,}000$ Hz, $N_c = 1$, $F_1 = 1$ Hz.

   (b) Localisation of the test signal's first local maximum $n_{\max,1,k}$.

   (c) Linear interpolation of the test signal amplitudes such that $n_{\max,1,k} \mapsto n_{\max,1,r}$ yields the interpolated test signal $y[n]$. This step is necessary because the location of the maximum point $n_{\max,1,k}$ is related to θ_k and therefore, in general, not equal to $n_{\max,1,r}$.

   (d) Evaluation of the mean-square error

$$e_{\alpha,k} = \frac{1}{n_{\max,1,r} + 1} \sum_{n=0}^{n_{\max,1,r}} \left(y[n] - s_r[n]\right)^2 \ .$$

3. Summation up of the step errors $e_{\alpha,k}$ yields the total error e_α.

4. Repetition of the loop for the variation ranges of β and γ returns the total errors e_β and e_γ. Finally, these errors are normalised to the maximum value of the total errors.

The corresponding analysis results can be found in Fig. 9, p. 38. See also function file[30] `algo_pdev.m`.

Detection parameter optimisation. Since the descriptions of the detection methods already include the optimisation settings and procedures, these are only summarised here.

- Optimisation settings: paragraph 'Detection parameter optimisation settings', p. 17
- Method LA, LAC, LR, LRC: paragraph 'Detection and error correction approach', p. 17 (step **A2**, **A3**)
- Method DH, DHC: paragraph 'The comparison methods DH and DHC', p. 19 (step **B2**, **B3**)
- Method SW, SWC: paragraph 'The comparison methods SW and SWC', p. 23 (step **C3**, **C4**)

The corresponding realisation of the procedure is available in the function file[30] `algo_part_2.m`. It is worth noting that the detection parameters are related to the signal model parameters α, β, and γ of the test signals. These are related to the physical model of the ultrasonic test configuration and the testing materials. Therefore, the procedure was carried out for all signal model parameter sets tabulated in Tab. 4, p. 36.

The optimisation results corresponding to the predefined signal model parameters as used for the sensitivity analysis can be found in Fig. 10, p. 39, Fig. 11, p. 40 and Tab. 5, p. 38. Furthermore, the optimisation results used for the onset point detection concerning natural signals from four different test series are tabulated in the Appendix section of this paper in Tab. 6, p. 58, Tab. 7, p. 59, Tab. 8, p. 59 and Tab. 9, p. 60.

Sensitivity analysis. The sensitivity analysis is intended to test the detection methods against synthetic test signals with additive noise. Therefore, the method's detection errors are computed by carrying out three different parameter variations concerning frequency and SNR employing several MCSs on the test signals s_t (eq. 5) and x_t (eq. 6). The entire sensitivity analysis relies on the initially optimised detection parameters (see Tab. 5, p. 38) related to the predefined signal model parameters (see eq. 3), $F_s = 10$ MHz, $N_{c,z} = 1$ and $N_c = 3$. The resulting detection errors from the MCSs allow for assessing the method's properties (metrics) in terms of robustness, complexity, accuracy and precision. The analysis procedure of the sensitivity analysis consists of the following steps:

1. Two-dimensional parameter variation concerning the parameters frequency and SNR based on the parameter ranges defined in eq. 10, eq. 11 and a resolution of $N_{\mathrm{var}} = 20$ points in each dimension (dimension indices i, j). For each parameter pair $p_{ij} = (F_{1,i}, \mathrm{SNR}_j)$, a MCS with $N_{\mathrm{MC}} = 100$ turns is carried out, returning the detection error sets X_{ij} and the computation time spans T_{ij}. From X_{ij} the following method properties are derived:
   - Sensitivity S_{ij} (eq. 60) for each parameter pair p_{ij}, normalised to the maximum magnitude $S_{ij,\max}$. See Fig. 12, p. 41.
   - Complexity C (eq. 62) based on all T_{ij} of the variation. C is normalised to the all-methods maximum magnitude $C_{\max}$. See Fig. 16, p. 44.

2. One-dimensional parameter variation concerning the frequency range defined in eq. 10, the fixed $\mathrm{SNR}_{\mathrm{low}} = 20$ dB and a resolution of $N_{\mathrm{var}} = 20$ points (dimension index i). For each parameter pair $p_{i1} = (F_{1,j}, \mathrm{SNR}_{\mathrm{low}})$, a MCS with $N_{\mathrm{MC}} = 1{,}000$ turns is carried out delivering the detection error sets X_{i1}. From that results the following method properties are derived:

   - Error distribution characteristics of X_{i1} for each parameter pair p_{i1}. The distributions are characterised by mean value, minimum, maximum, and the quantiles $q_{0.05}$, $q_{0.25}$, $q_{0.75}$, $q_{0.95}$. See Fig. 13, p. 42.
   - Robustness score R (eq. 61) with $X = \bigcup_{i=1}^{N_{\mathrm{var}}} X_{i1}$. See Fig. 15 (a), p. 44.

3. One-dimensional parameter variation concerning the SNR range defined in eq. 11, the fixed $\mathrm{F}_{1,\mathrm{low}} = 5$ kHz and a resolution of $N_{\mathrm{var}} = 20$ points (dimension index j). For each parameter pair $p_{1j} = (\mathrm{F}_{\mathrm{low}}, \mathrm{SNR}_j)$, a MCS with $N_{\mathrm{MC}} = 1{,}000$ turns is carried out delivering the detection error sets X_{1j} from which the following properties are derived:

   - Error distribution characteristics of X_{1j} for each parameter pair p_{1j}. The distributions are characterised by mean value, minimum, maximum, and the quantiles $q_{0.05}$, $q_{0.25}$, $q_{0.75}$, $q_{0.95}$. See Fig. 14, p. 43.
   - Robustness score R (eq. 61) with $X = \bigcup_{j=1}^{N_{\mathrm{var}}} X_{1j}$. See Fig. 15 (b), p. 44.

4. A single MCS for the parameter point $p_{11} = (F_{\mathrm{low}}, \mathrm{SNR}_{\mathrm{low}})$ with $N_{\mathrm{MC}} = 1{,}000$ turns, delivers the detection error set X_{11} from which the following properties are derived:

   - Homogeneity of X_{11} concerning the normal distribution using the χ^2-test as explained in subsection 'Performance standards and metrics', p. 24. See Fig. 19, p. 45.
   - Accuracy A related to μ (eq. 63) and precision P related to σ (eq. 64) of X_{11}. See Fig. 18, p. 45.

5. Performance assessment based on the composite metrics score S (eq. 66) employing the method metrics complexity C (eq. 62), accuracy A (eq. 63) and precision P (eq. 64). For certain applications the method's complexity might not be of interest. Therefore, for the method's composite performance score two different situations are considered: (1) S_{CAP} considering the complexity and (2) S_{AP} without considering the complexity. See Fig. 20, p. 45.

See also function file[30] `algo_part_3.m`.

Onset point error estimates concerning natural signals. The onset point error estimates for natural ultrasound signal data are intended to demonstrate that the methods do not only apply to a theoretical signal model, but also to natural signals from laboratory tests. The error estimates are, therefore, compiled for all datasets listed in Tab. 1, p. 9. First, the onset point $\hat{n}_{0,f}$ is estimated with the semi-automated procedure described in paragraph 'Parametrisation of the signal model', p. 27. These estimates serve as a reference for the

exact solution and represent the basis for the error estimates (eq. 56, eq. 57). Additionally, the signal frequency and the SNR are estimated. That estimates allow to validate the initially defined value ranges (eq. 10, eq. 11) used for the sensitivity analysis.

The analysis procedure is applied iteratively on the signal sequence consisting of K signals, descending from the largest to the smallest signal index. This approach is particularly beneficial for the signal series of Test series 1 (cement paste). After 24 hours (signal index $k = K$), the cement paste has already hardened. Thus, the signal amplitudes are large and the noise amplitudes are small. That measure increases the stability of the subsequent analysis because the previous results can be used as estimates for the current analysis (e.g., step 3 or step 7).

The analysis procedure for the k^{th} signal x from the sequence of signals consists of the following steps:

1. Selection of the k^{th} signal x from the signal sequence and the detection parameters corresponding to the actual testing material (actual test series). The corresponding detection parameters can be found in Tab. 6, p. 58, Tab. 7, p. 59, Tab. 8, p. 59 and Tab. 9, p. 60.

2. De-trending of x by estimating the constant bias

$$\hat{b} = \frac{1}{|w_\nu|} \sum_{(w_\nu)} x[n] \tag{78}$$

   using the noise measuring window w_ν (eq. 16), and subtracting the bias from the signal yields the de-trended signal

$$x_d[n] = x[n] - \hat{b}, \quad 0 \leq n \leq N-1\,. \tag{79}$$

3. Estimation of the a priori SNR measuring window w_1. If $k = K$, $w_1 = w_{1,1}$ (eq. 19), $w_1 = w_{1,1}$ (eq. 20) otherwise. The onset point estimate $\hat{n}_0$ used to define $w_{1,2}$ is determined by the all-methods minimum of the previous $(k+1)$ onset point location estimates n_x or $\hat{n}_0$.

4. A priori SNR estimate SNR1 (eq. 28) based on the noise measuring window w_ν (eq. 16), the signal power measuring window w_1 from the previous step and the de-trended signal x_d (eq. 79). See also paragraph 'SNR estimates', p. 13.

5. Check whether the termination condition SNR1 $\leq$ 20 dB is met. If this is the case, the detection limit $k_{\text{lim}} = k + 1$ is updated and the iteration loop over the signal sequence is aborted.

6. Filtering of x_d as an additional preconditioning measure for the local maximum detection and the frequency range estimates returns $x_{d,f}$. See also paragraph 'Finite Impulse Response (FIR) filter', p. 14.

7. Detection of the first local maximum' location

$$n_{\max,1} \leftarrow \begin{cases} \textsc{DetInitMax}(x_m, w_1), & k = K \\ \textsc{DetLocMax}(x_m, w_1, c_{\text{lim}}, L_{\text{rng}}), & k < K \end{cases} \tag{80}$$

with the detection range length $L_{\mathrm{rng}} = 5000$ samples and the counter limit $c_{\mathrm{lim}} = \hat{n}_{xc,k+1} - n_{\mathrm{max},1,k+1}$ samples. The filtered signal $x_m = x_{d,f}$ is only used in case of SNR1 ≤ 20 dB, otherwise the maximum point detection is applied to the unfiltered signal $x_m = x_d$. See also paragraph 'Local maximum detection', p. 16.

8. Localisation the first x-axis crossing n_{xc} behind the first local maximum point using $n_{\mathrm{max},1}$ as a starting point for a forward search. To increase the accuracy of the detection results for coarsely sampled signals, a linear interpolation between the samples around the x-axis crossing yields $\hat{n}_{xc}$.

9. Detection stabilisation by setting the signal amplitudes in the index range in front of the signal power measuring window w_1 to zero, which returns $x_{d,z}$. This measure suppresses the signal amplitudes in the electromagnetic response section.

10. Normalisation of $x_{d,z}$ to the first local maximum's amplitude $x_{d,z}|_{n_{\mathrm{max},1}}$ returns $\hat{x}$.

11. Application of all detection methods on $\hat{x}$. The detection results deliver the onset point locations n_x or $\hat{n}_0$ and the corresponding detection errors $e_{\mathrm{det},x}$ (eq. 56) and $e_{\mathrm{det},c}$ (eq. 57). A by-product of the detection is the secant's gradient c_1, which allows for an additional frequency estimate (see next step). If a detection error occurs, the signal index $k_{\mathrm{lim}} = k + 1$ defines the detection limit, and the iteration loop over the signal sequence is aborted.

12. Estimation of the the signal model's primary frequency

$$\hat{F}_1 \approx F_s \, \frac{c_1 - k_0}{k_1} \tag{81}$$

by transforming the relation between the signal model's normalised frequency F_1/F_s and the secant's gradient c_1 (eq. 41).

13. Estimation of the measuring window w_2 (eq. 23). The onset point estimate $\hat{n}_0$ used to define w_2 is determined by the minimum of the current onset point location estimates n_x or $\hat{n}_0$ of all methods.

14. The a posteriori SNR estimate delivers SNR2 (eq. 29) based on the preconditioned signal x_d and the signal power measuring window w_2 (eq. 23). See also paragraph 'SNR estimates', p. 13.

15. Check whether the termination condition SNR2 ≤ 20 dB is met. If this is the case, the detection limit $k_{\mathrm{lim}} = k + 1$ is updated and the iteration loop over the signal sequence is aborted.

16. Frequency range estimation based on $x_{d,f}$ and the window w_2 (see also paragraph 'Frequency range estimates', p. 15).

17. If $k = K - 1$, repeat the steps 1 to 7 for the last signal x_K in the sequence. This step is performed to update the initial estimates for SNR1 and $n_{\mathrm{max},1}$ of the sequence' last signal.

Exemplary analysis results for selected data sets of test series 1 (cement paste) can be found in the Appendix section of this paper in Fig. 26, p. 62, Fig. 27, p. 63 and Fig. 28, p. 64. See also function file[30] `algo_part_4.m`.

Statistics related to the analysis of natural signals. From the analysis of all data sets under consideration (see also Tab. 1, p. 9) several statistics emerge. These are compiled for each test series (each material type), but also for the combination of all test series to get an overall picture. First, the i^{th} signal's metric M_{ijk} (e.g., detection error) is accumulated for all data sets j of a test series k, which yields the sample $X_k = \bigcup_{j=1}^{J_k} \bigcup_{i=1}^{I_j} M_{ijk}$. Second, these samples are accumulated for all test series k, which yields the sample $X = \bigcup_{k=1}^{K} X_k$ with the number of successfully analysed signals I_j of a signal sequence in a dataset, the number of data sets in a test series J_k and the number of test series $K = 4$. Based on that samples, the following metrics are evaluated:

- Onset point detection error statistics for all methods based on the detection error (eq. 56 or eq. 57) for each detection method m. The samples $X_{k,m}$ and X_m are characterised by minimum, maximum, median and the quantiles $q_{0.05}$, $q_{0.25}$, $q_{0.75}$, $q_{0.95}$. See also Fig. 21, p. 46.

- Robustness score statistics for all methods based on the detection error (eq. 56 or eq. 57) for each detection method m using the samples $X_{k,m}$ and X_m of the above-described onset point detection error statistics. The robustness scores $R(X_{k,m})$ and $R(X_m)$ are evaluated according to equation eq. 60 and eq. 61 (normalised inverted metric score). See also Fig. 22, p. 46.

- Frequency range statistics. The signal frequency estimates (metrics $M_{ijk,m}$) are delivered by three different methods m: (1) DFT based ($q_{0.05}$ and $q_{0.95}$ quantiles of the PSD's cumulative sum); (2) based on the secant gradients of method LA and LR (eq. 81); (3) curve fitting (see paragraph 'Parametrisation of the signal model', p. 27). In general, the frequency ranges are characterised by the minimum and maximum values of the samples $X_{k,m}$ and X_m. Solely, the DFT-based frequency range estimates are handled differently: $(F_{k,\min}, F_{k,\max}) = (\min X_{k,q_{0.05}}, \max X_{k,q_{0.95}})$ and $(F_{\min}, F_{\max}) = (\min X_{q_{0.05}}, \max X_{q_{0.95}})$. Using the quantiles instead of the extreme values, avoids considering outliers. See also Fig. 23, p. 47.

- SNR range statistics based on the a priori and a posteriori SNR estimates m (SNR1, SNR2). As for the frequency range statistics, the samples $X_{k,m}$ and X_m are characterised by the minimum and maximum value. See also Fig. 24, p. 47.

See also function file[30] `algo_stats.m`.

After this admittedly technical and dry methods section, the inclined reader now deserves to see something more colourful – the analysis results.

3 Results

From the analysis procedures, a series of illustrations emerges. These are summarised in this section, allowing for a better understanding of how the above-described detection methods behave. The order of the their appearance also guides the reader through the story.

First, it is demonstrated that the proposed signal model adapts well to natural signals within the detection zone. Then, the method's detection parameter

optimisation according to that signal model follows. Now, everything is in place to examine the detection methods' behaviour. The sensitivity analysis exhibits the method's properties and behavioural patterns concerning robustness to frequency and noise, the computational effort, and the achievable accuracy and precision. After these first insights, the focus shifts towards natural signals for demonstrating that the detection methods apply to these signals as well. A variety of ultrasound signals originating from ultrasound tests using different testing materials and measuring distances are analysed. Finally, the analysis results allow for comparing the methods' behaviour concerning synthetic and natural signals.

Data sets	Description	α	β	γ
Test series 1	cement paste	2.12	0.05	0.7
Test series 5	ambient air	2.14	0.35	1.63
Test series 6	tap water	1.84	0.15	1.74
Test series 7	aluminium cylinder	1.74	0.12	0.83
Combined	all materials	2.1	0.07	0.76
—	predefined values	2	0.5	1.5

Table 4: Signal model fitting results. Median values of the signal model parameters as shown in Fig. 8, p. 37 (b), (d) and (f).

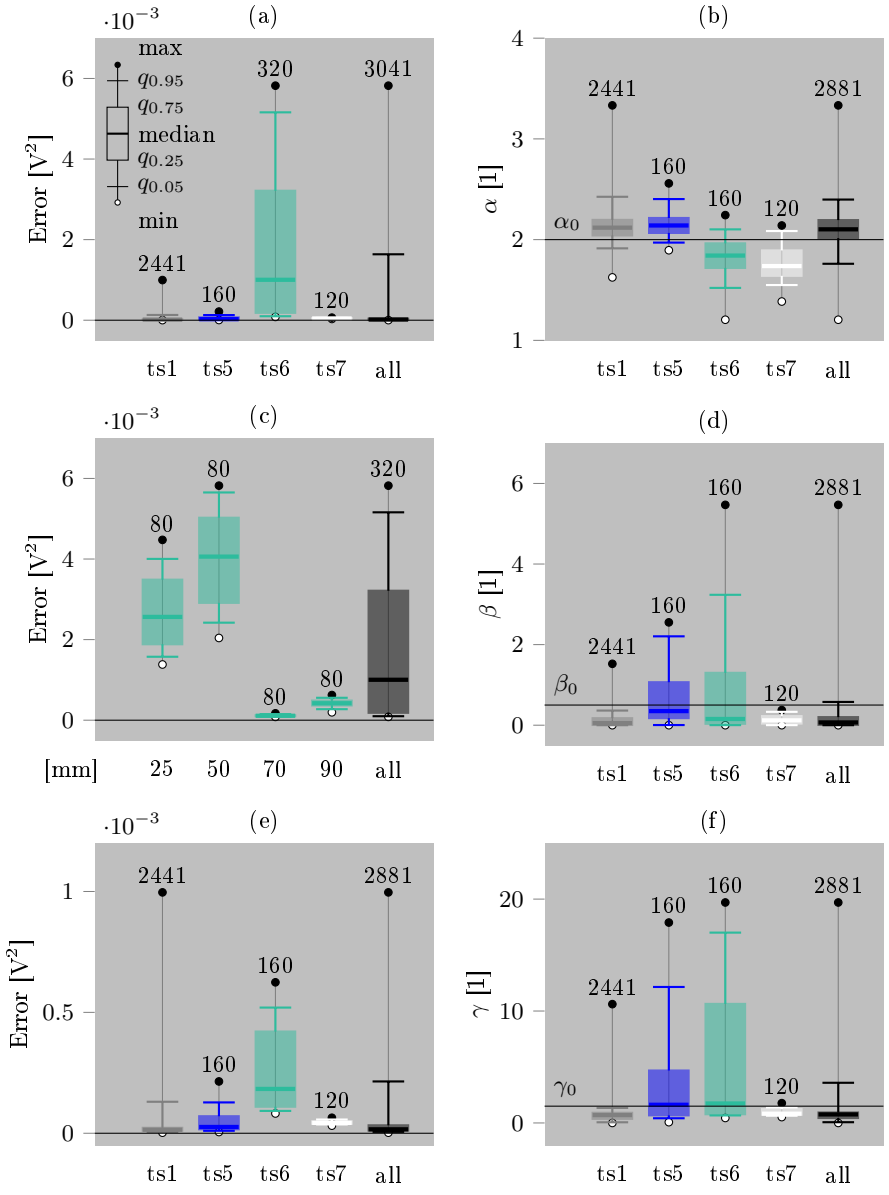

Figure 8: Signal model parameter distributions and fitting error statistics concerning natural signals. **(a)** fitting error (all data sets from all test series, see Tab. 1, p. 9). **(b)** frequency ratio α. **(c)** fitting error (data sets from test series 6 only). **(d)** primary damping factor β. **(e)** fitting error (without the data sets from test series 6 concerning the UMDs 25 and 50 mm). **(f)** secondary damping factor γ. *Note:* The number above the maximum dots represents the sample size N (number of signals). *Legend:* ts1 ... test series 1, cement paste; ts5 ... test series 5, ambient air; ts6 ... test series 6, tap water; ts7 ... test series 7, aluminium cylinder.

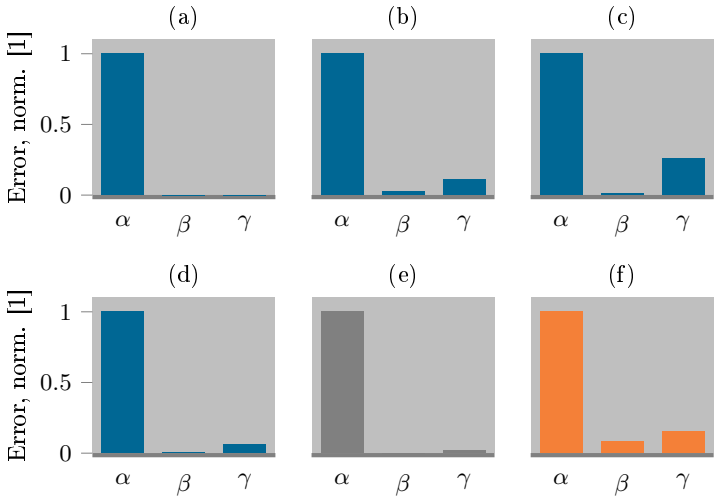

Figure 9: Sensitivity concerning deviations (±20 %) in the signal model parameters. **(a)** test series 1. **(b)** test series 5. **(c)** test series 6. **(d)** test series 7. **(e)** all test series combined. **(f)** predefined values. *Note:* The signal model parameters related to each panel are tabulated in Tab. 4, p. 36.

Signal model parameters			
Parameter	α	β	γ
Value	2	0.5	1.5
Secant detection parameters			
Method	t_0	t_1	t_2
LA, LAC	0.556	0.200	0.912
LR, LRC	0.558	0.183	0.933
DH, DHC	0.525	0.350	0.700
SW, SWC	0.556	0.200	0.912
Sliding window parameters			
Method	t_v	t_w	
SW, SWC	0.500	0.355	
Error correction parameters			
Method	$t_{c,0}$	$t_{c,1}$	
LAC	0.640	−0.443	
LRC	0.689	−0.591	
DHC	0.080	−0.092	
SWC	−0.000	−1.977	

Table 5: Detection parameters optimised concerning the predefined signal model parameters. *Legend:* t_0 ... initial threshold; t_1 ... lower threshold; t_2 ... upper threshold; t_v ... voltage threshold; t_w ... window fill threshold; $t_{c,0}$, $t_{c,1}$ ... monomial coefficients of the correction threshold polynomial $t_{c,\mathrm{app}}$; the number in the subscript refers to the monomial's power.

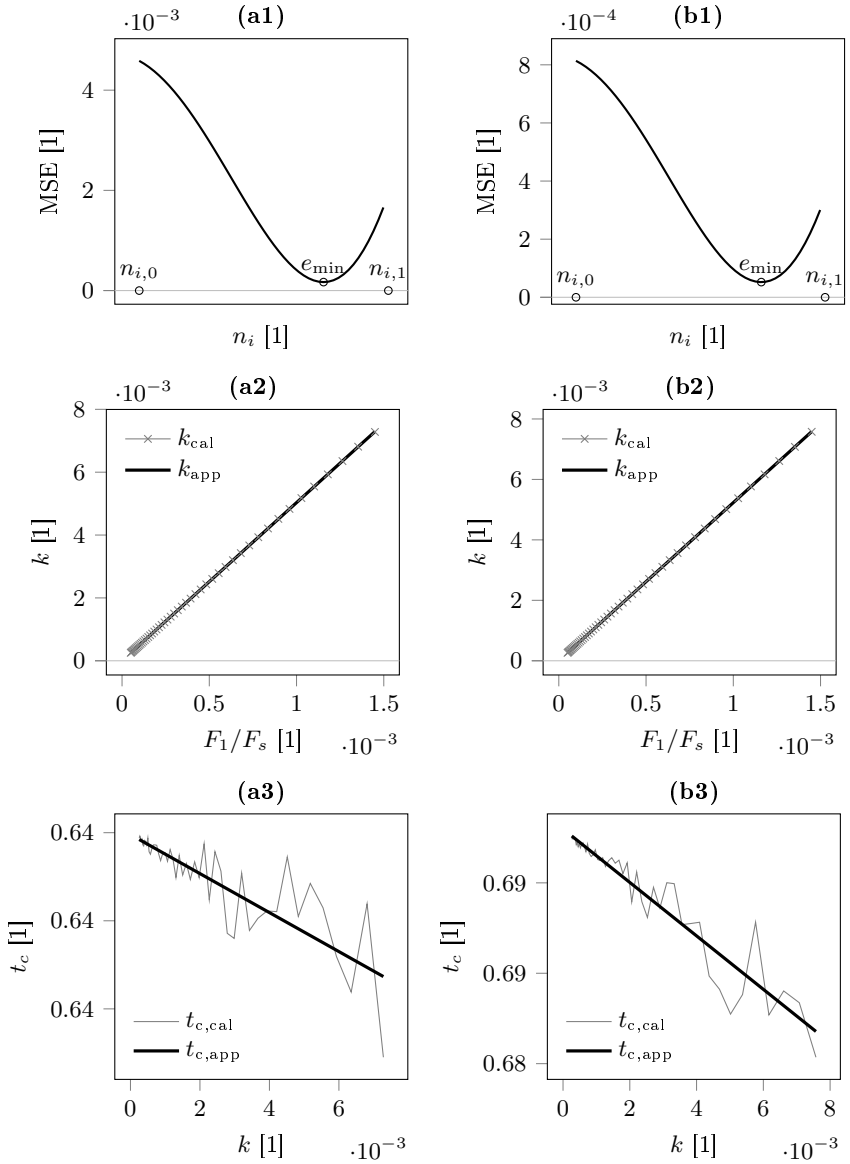

Figure 10: Detection parameter optimisation results related to method LA, LAC, LR and LRC and the predefined signal model parameters. **(a1)** LA, secant fitting error. **(a2)** LAC, $F_1/F_s \sim k$. **(a3)** LAC, $t_c \sim k$. **(b1)** LR, secant fitting error. **(b2)** LRC, $F_1/F_s \sim k$. **(b3)** LRC, $t_c \sim k$. *Note:* The subscript $(\,)_{\text{cal}}$ denotes the calculated variation results and $(\,)_{\text{app}}$ the linear approximation of $(\,)_{\text{cal}}$.

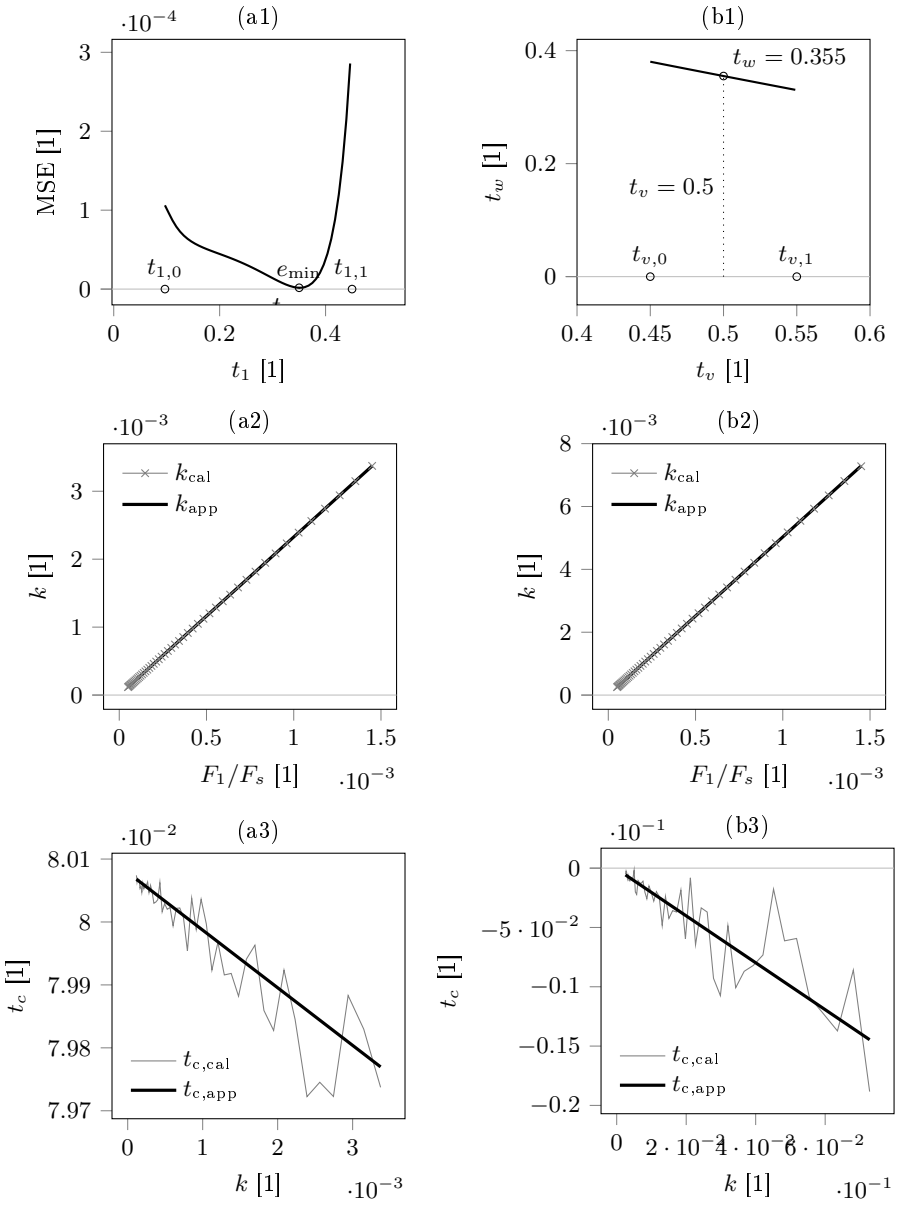

Figure 11: Detection parameter optimisation results related to method DH, DHC, SW and SWC and the predefined signal model parameters. **(a1)** DH, secant fitting error. **(a2)** DHC, $F_1/F_s \sim k$. **(a3)** DHC, $t_c \sim k$. **(b1)** SW, $t_v \sim t_w$. **(b2)** SWC, $F_1/F_s \sim k$. **(b3)** SWC, $t_c \sim k$. *Note:* The subscript $(\,)_{\text{cal}}$ denotes the calculated variation results and $(\,)_{\text{app}}$ the linear approximation of $(\,)_{\text{cal}}$.

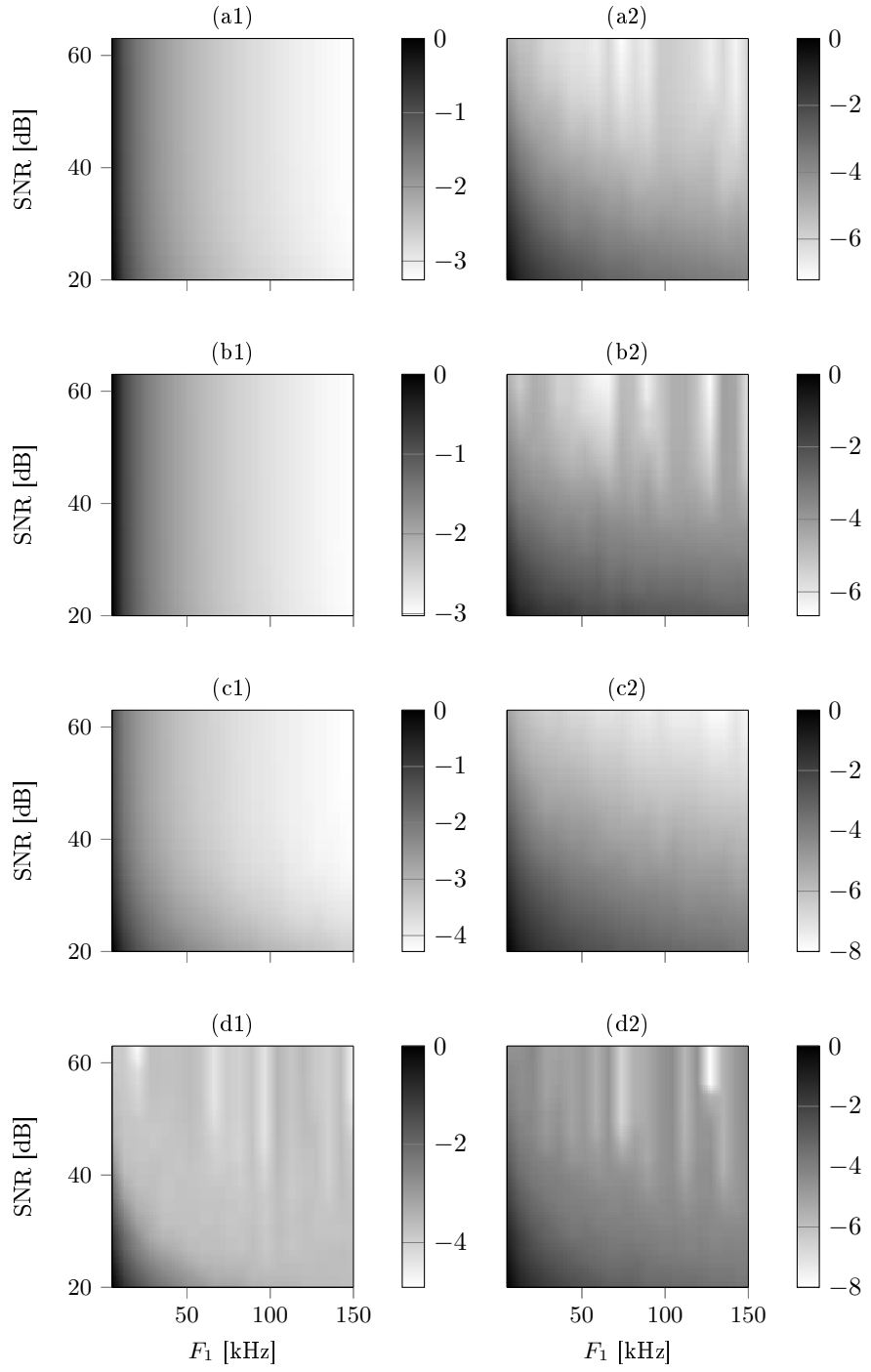

Figure 12: Sensitivity to frequency and SNR (normalised to the maximum magnitude, $\log_{10}$-scale). $N_{\mathrm{MC}} = 100$, $N_{\mathrm{var}}^{F_1} = N_{\mathrm{var}}^{\mathrm{SNR}} = 20$. **(a1)** LA. **(a2)** LAC. **(b1)** LR. **(b2)** LRC. **(c1)** DH. **(c2)** DHC. **(d1)** SW. **(d2)** SWC.

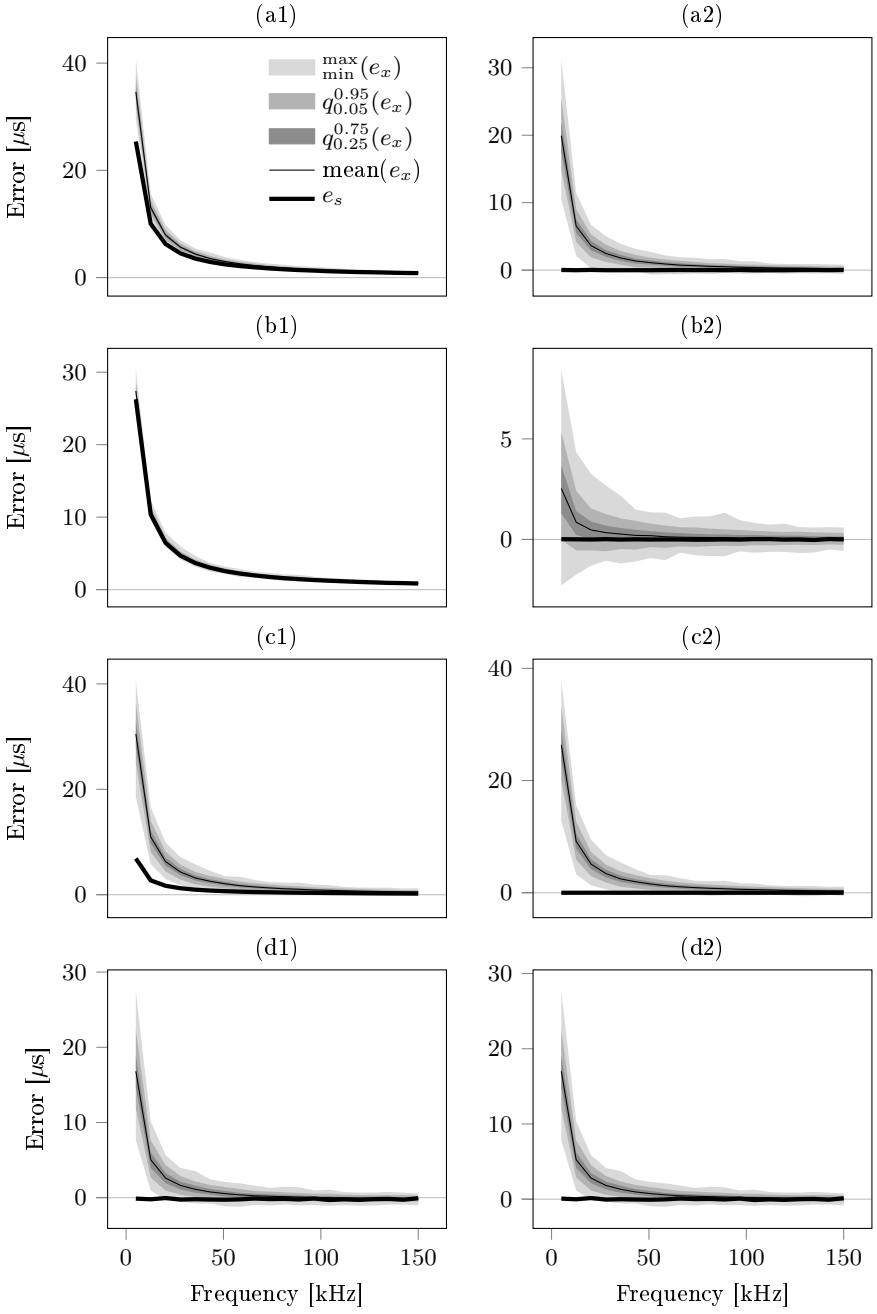

Figure 13: Onset point detection error distributions concerning the frequency. $N_{\mathrm{MC}} = 1000$, $N^{F_1}_{\mathrm{var}} = 20$, SNR = const. = 20 dB. **(a1)** LA. **(a2)** LAC. **(b1)** LR. **(b2)** LRC. **(c1)** DH. **(c2)** DHC. **(d1)** SW. **(d2)** SWC. *Legend:* e_s ... error estimates, clean signal; e_x ... error estimates, signal corrupted by noise; $q^{0.95}_{0.05}(e_x)$, $q^{0.75}_{0.25}(e_x)$ ... quantile ranges.

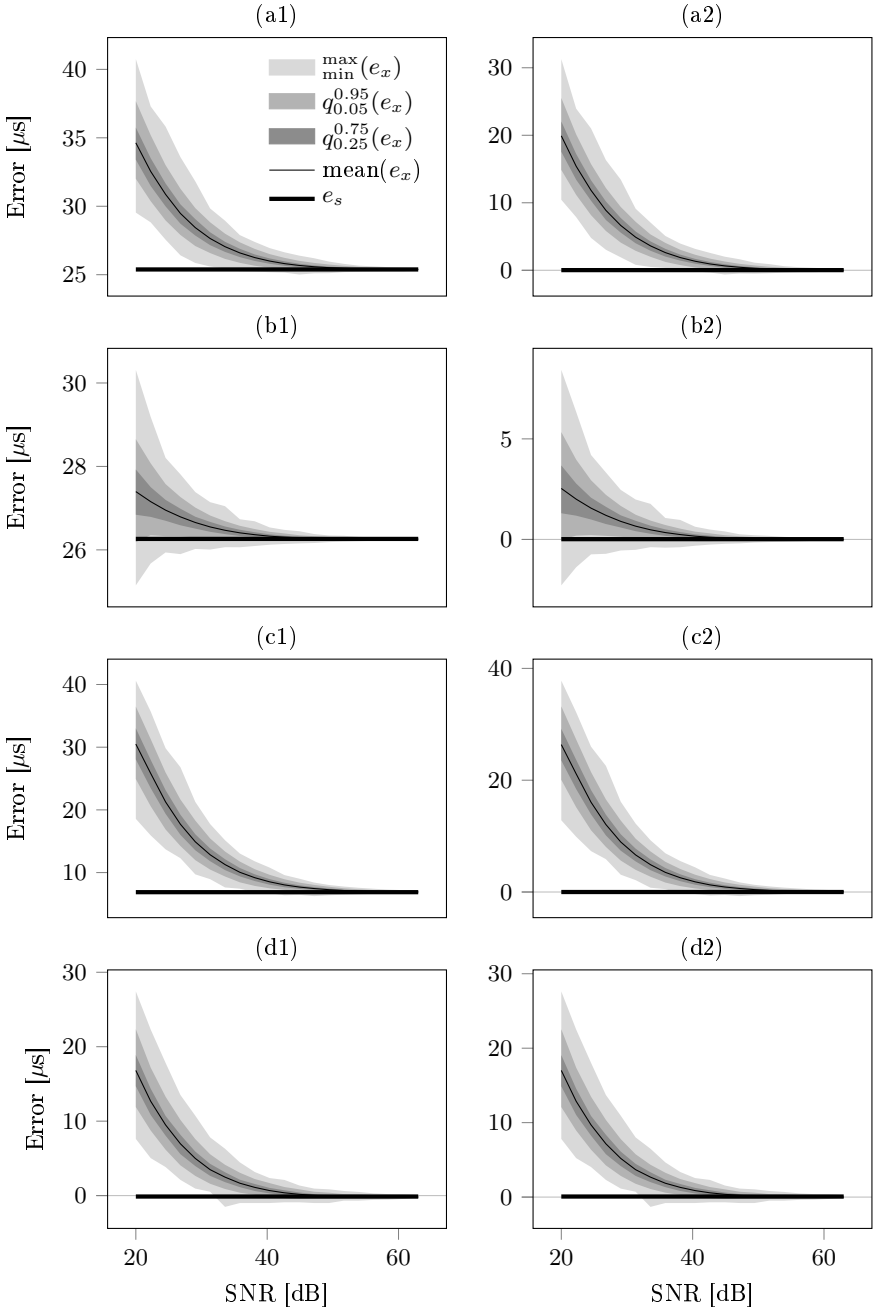

Figure 14: Onset point detection error distributions concerning the SNR. $N_{\mathrm{MC}} = 1000$, $N_{\mathrm{var}}^{\mathrm{SNR}} = 20$, $F_1 = \mathrm{const.} = 5$ kHz. **(a1)** LA. **(a2)** LAC. **(b1)** LR. **(b2)** LRC. **(c1)** DH. **(c2)** DHC. **(d1)** SW. **(d2)** SWC. *Legend:* e_s ... error estimates, clean signal; e_x ... error estimates, signal corrupted by noise; $q^{0.95}_{0.05}(e_x)$, $q^{0.75}_{0.25}(e_x)$ ... quantile ranges.

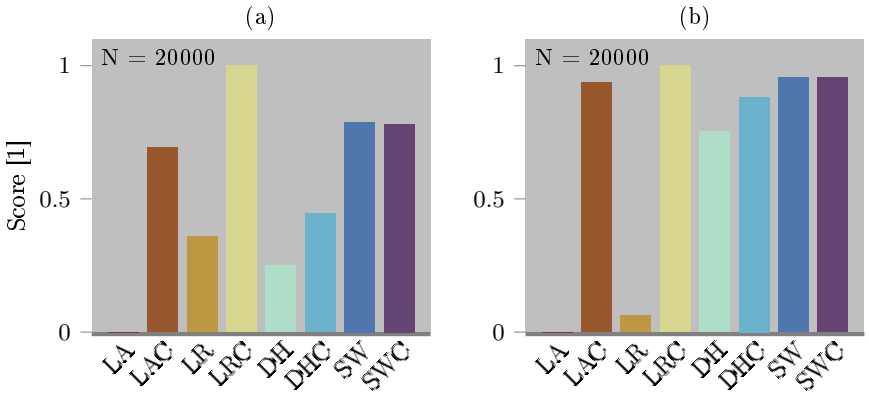

Figure 15: Robustness to frequency and noise (normalised and inverted sensitivity). **(a)** robustness to frequency. **(b)** robustness to noise.

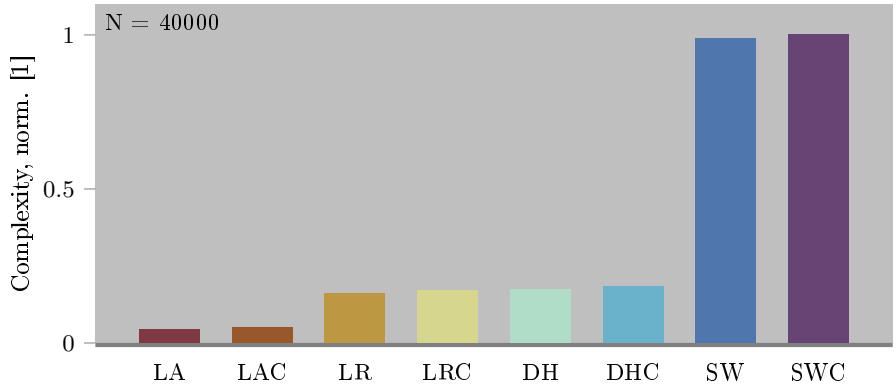

Figure 16: Complexity score (normalised to the maximum magnitude).

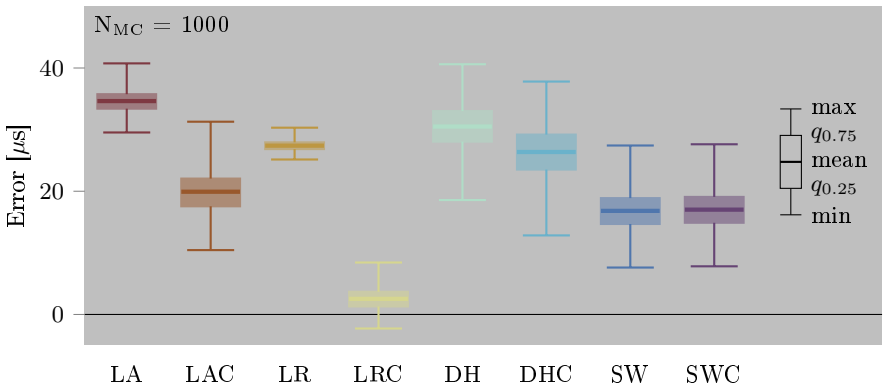

Figure 17: Onset point detection error distributions at the lower limits of frequency and SNR ($F_1 = 5$ kHz, SNR $= 20$ dB).

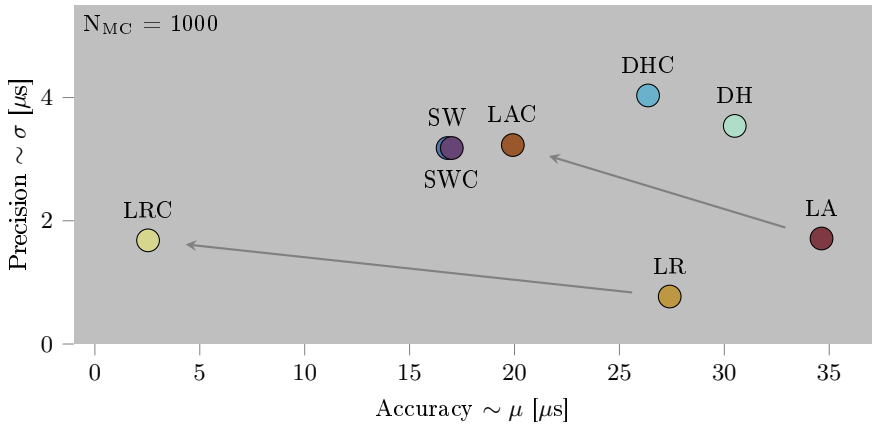

Figure 18: Accuracy and precision at the lower limits of frequency and SNR ($F_1 = 5$ kHz, SNR = 20 dB).

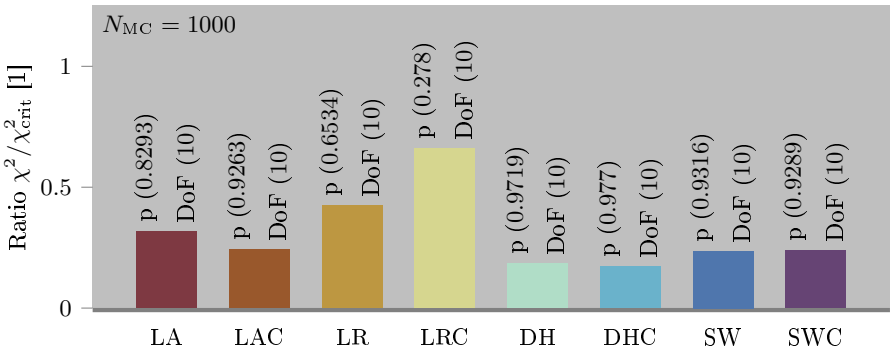

Figure 19: Homogeneity of the detection error distributions concerning the normal distribution at the lower limits of frequency and SNR ($F_1 = 5$ kHz, SNR = 20 dB). *Legend:* p ... p–value; DoF ... degrees of freedom, χ^2-test.

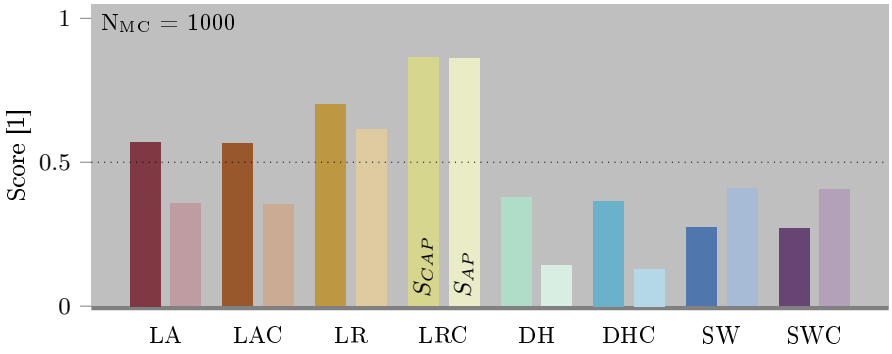

Figure 20: Performance concerning the metrics complexity C, accuracy A and precision P (composite inverted metrics score). *Legend:* S_{CAP} ... score, considering all three metrics; S_{AP} ... score, considering accuracy and precision only.

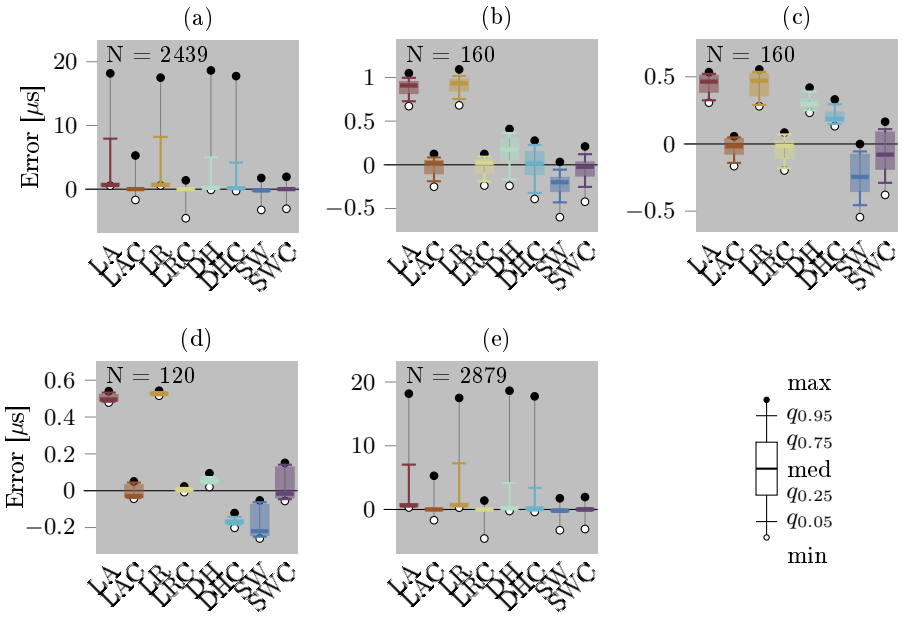

Figure 21: Onset point detection error distributions concerning natural signals. **(a)** Test series 1, cement paste. **(b)** Test series 5, ambient air. **(c)** Test series 6, tap water. **(d)** Test series 7, aluminium cylinder. **(e)** all test series combined.

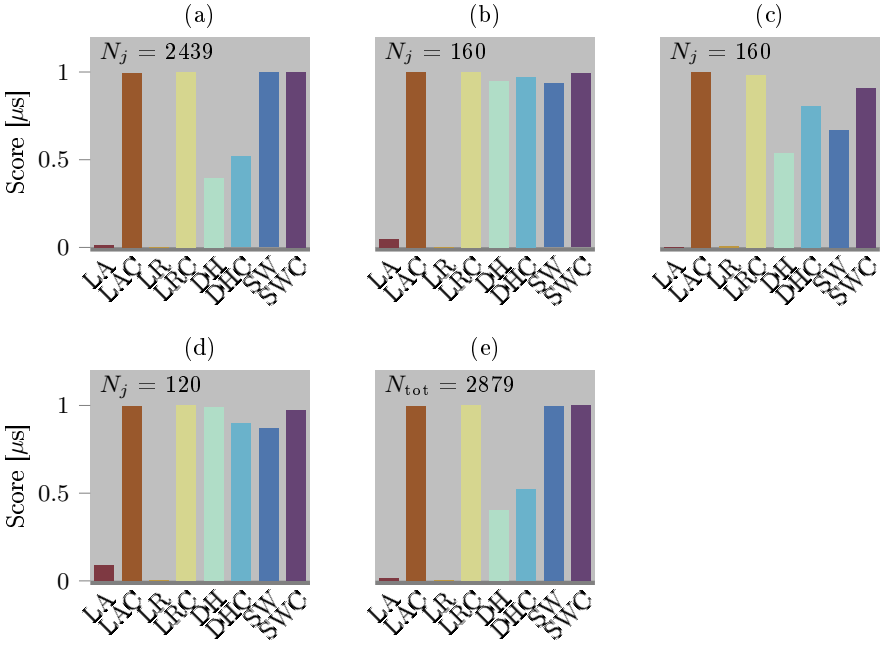

Figure 22: Robustness concerning natural signals. **(a)** Test series 1, cement paste. **(b)** Test series 5, ambient air. **(c)** Test series 6, tap water. **(d)** Test series 7, aluminium cylinder. **(e)** all test series combined.

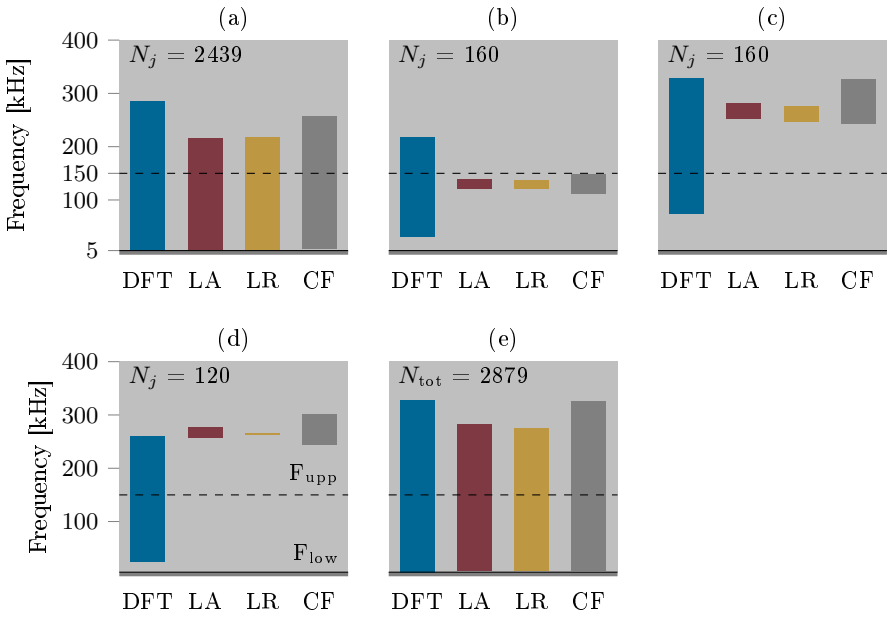

Figure 23: Frequency range estimates concerning natural signals (min/max of the quantiles $q_{0.05}$ and $q_{0.95}$). **(a)** Test series 1, cement paste. **(b)** Test series 5, ambient air. **(c)** Test series 6, tap water. **(d)** Test series 7, aluminium cylinder. **(e)** all test series combined. *Legend:* F_{res} ... resonance frequency of the piezoelectric sensors; SF ... curve-fitting.

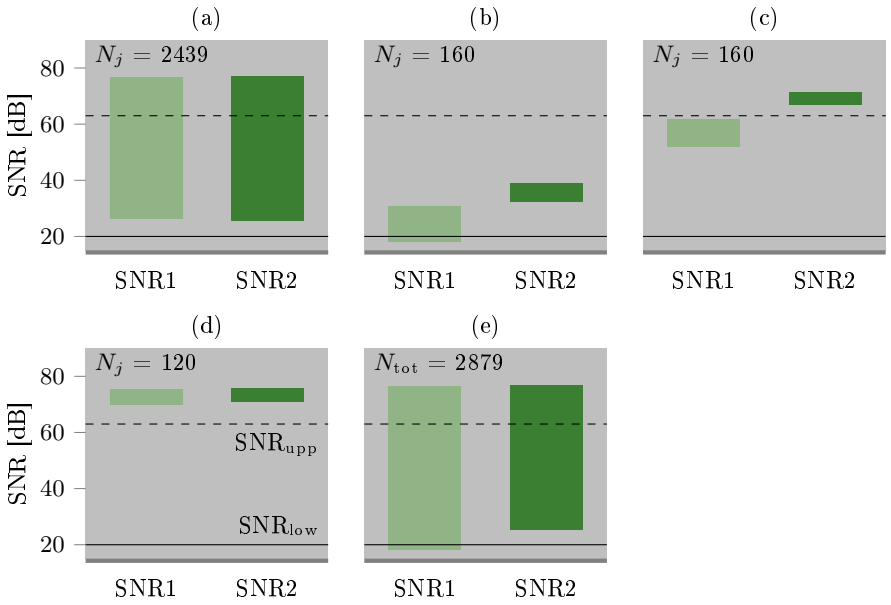

Figure 24: SNR range estimates concerning natural signals (min/max values). **(a)** Test series 1, cement paste. **(b)** Test series 5, ambient air. **(c)** Test series 6, tap water. **(d)** Test series 7, aluminium cylinder. **(e)** all test series combined.

4 Discussion

Based on the analysis methods defined in section 'Materials & Methods', p. 5 and the corresponding analysis results illustrated in section 'Results', p. 35, a discussion can take place. In this discussion, particular attention is paid to the method's detection parameter optimisation, enabling systematic error correction, reduction of computational effort, robustness to frequency and noise, and the achievable accuracy and precision, as well as the applicability domains. However, the discussion primarily addresses the core methods LA, LAC, LR and LRC of this paper. These are compared to the methods DH, DHC, SW and SWC derived from the existing literature.

The signal model enabling systematic error correction. The optimisation of the detection parameters to a specific signal model (eq. 2) is at the core of the methods LAC and LRC and enables systematic error correction. By showing that the signal model fits well to natural signals in the detection zone, the detection parameters optimised with respect to that signal model can then be subjected to the analysis of natural signals.

As can be seen in the curve fitting results (Fig. 8, p. 37, Tab. 4, p. 36), the proposed signal model (eq. 2) adapts quite well to the vast majority of signals. The counterexamples (see Fig. 8 (c), p. 37) related to a couple of data sets of test series 6 prove the rule (tap water, UMD 25 and 50 mm). Excluding these data sets from the statistics reduces the fitting error (Fig. 8 (e), p. 37, ts6) by a factor of ten. As can be seen in Fig. 25 (g), (h), p. 61 and Tab. 10, p. 60, the proposed signal model is not suitable for this kind of signals who's shape notably differs from the proposed signal model.

From the curve-fitting results, it also becomes apparent that the signal model parameters vary across different ranges for different testing materials. That underpins the assumption that these parameters are related to specific physical models. Thus, it makes sense to optimise the detection parameters for each testing material as this is one of the fundamental components of the testing device's physical model. In this paper, the analysis of natural signals related to the four different materials, therefore, relies on different signal model parameters (Tab. 4, p. 36) and their corresponding detection parameters (Tab. 6, p. 58, Tab. 7, p. 59, Tab. 8, p. 59, Tab. 9, p. 60).

Related to that, it is interesting to note (Fig. 9, p. 38) that the signal model parameters have different impact on the signal's shape within the detection zone. Regardless of material type and measuring distance, the parameter α (frequency ratio) is the governing factor, followed by γ (secondary damping factor) and β (primary damping factor). From that, it becomes apparent that optimising the parameter α is of utmost importance, while the other two parameters play a subordinate role.

The predefined value of α (eq. 3) is aiming to represent the average behaviour of all investigated data sets (Tab. 1, p. 9) concerning different testing materials (see Tab. 4, p. 36). Since the parameters β and γ play a subordinate role, the remaining variable is the signal model's primary frequency F_1. That circumstance is utilised in the sensitivity analysis by only varying F_1 instead of all parameters. Due to the definition of the signal model, the signal model's period scales with F_1 only, as is the case for a simple sine function.

Although the adaptation of the signal model is effective for various signals, the fitting yields minor errors solely in the detection zone. Beyond the primary wave's first local maximum, the signal model deviates remarkably from the shape of natural signals. Despite these deviations, it is still possible to use the chosen signal model for optimisation and detection purposes because the detection of the primary waves's onset point happens exclusively in the area of the detection zone. That is precisely the region where the signal model fits best to the natural signal's shape.

The general picture of the curve-fitting results is that the signal model can be parametrised such that it fits a variety of different signals with a small error (Fig. 8 (e), p. 37). That gives rise for the assumption that the signal model represents an entire class of signals. As mentioned above, this behaviour is, of course, restricted to the detection zone. Thus, the actual shape of the signal is only related to the parametrisation. A reconstruction of the proposed signal model's definition concerning a specific material type is not necessary.

Optimisation of the detection parameters. As already mentioned in the introduction section, robustness to frequency and noise is the detection method's primary design goal and optimisation criterion. The optimisation of the detection parameters concerning the signal model $s[n, \theta)$ (eq. 2) is particularly targeted to compensate for the bias due to the magnitude of the threshold value and the signal's shape.

In the course of the optimisation of method LA, LAC, LR, and LRC, the signal is first replaced by a secant in the detection zone, which is accomplished either by the two-point form (LA, LAC), or by linear regression (LR, LRC). The x-axis crossing of the secant line provides the initial estimate for the primary wave's onset point. The systematic error correction, which takes advantage of the signal model's shape, yields the enhanced or corrected onset point estimate.

Due to the error minimisation approach utilised for the optimisation, it is necessary to show that the fitting error of the signal's secant assumes a minimum within the detection zone to ensure the uniqueness of the solution. As can be seen in Fig. 10 (a1), (b1), p. 39, that is indeed the case. Connected to that, the seemingly arbitrarily chosen length factor $f_{L,\mathrm{opt}} = 0.4$ defining the optimisation interval w_{opt} (eq. 18) is chosen just large enough such that the secant's gradient k and the signal model's normalised primary signal frequency F_1/F_s are directly proportional to each other (see Fig. 10 (a2), (b2), p. 39). Furthermore, the reverse relationship (eq. 81) allows for estimating the signal model's primary frequency $\hat{F}_1$ (eq. 81) when analysing natural signals (see Fig. 26 (f), p. 62, Fig. 27 (f), p. 63, Fig. 28 (f), p. 64, Fig. 23, p. 47).

Since the signal model's period scales with the primary frequency F_1 only, it is not a big surprise that the correction threshold t_c is also linearly related to the secant's gradient k (see Fig. 10 (a3), (b3), p. 39). It is worth mentioning that the visible oscillation of $t_{c,\mathrm{cal}}$ is because the secant support indices are integer values.

The optimisation of the comparison methods DH, DHC, SW and SWC follows the same principle as for the methods LA, LAC, LR and LRC. However, the comparison methods operate on a transformed signal or employ a sliding window. Thus, it is interesting to see that the correction threshold t_c is still related linearly to the secant's gradient k.

Robustness to frequency and noise. The detection parameter optimisation discussed above is targeted to cancel out the dependency to the signal's frequency. It is now to examine the methods sensitivity or robustness concerning frequency and noise.

First, it is important to see how the methods behave within the predefined variation ranges for frequency and noise (two-dimensional parameter range). As can be seen in Fig. 12, p. 41, for all methods the error is decreasing with increasing SNR. Regarding the frequency, the methods LA and LR exhibit a remarkable bias (Fig. 12 (a1), (b1), p. 41), which can be considerably reduced by systematic error correction (Fig. 12 (a2), (b2), p. 41). However, the general impression is that the detection error is high when frequency and SNR are low, which is expected.

This first impression is of course reflected in the results of the frequency variation (Fig. 13, p. 42) and the SNR variation (Fig. 14, p. 43), which represent the bottom border and the left border of the two-dimensional parameter range. However, the frequency variation (SNR = const. = 20 OTusesigsnr-low.u) exhibits that the influence of noise is decreasing with increasing frequency regardless of what method is used (Fig. 13, p. 42). At first glance, that may seem unexpected, but it is explainable. Increasing frequency means that the resolution of the first lobe of the incoming primary wave is decreasing. That loss of resolution has an effect similar to filtering. Thus, the influence of noise decreases as the frequency increases. Another side effect of low resolution is that the detection error, which is coupled with the secant's gradient converges towards zero as the resolution decreases.

The comparison of the method's robustness score (Fig. 15, p. 44) shows that the method LRC is most robust to frequency and noise. Concerning varying frequencies the difference to the other methods is most obvious (Fig. 15 (a), p. 44), but is considerably smaller concerning varying SNRs (Fig. 15 (b), p. 44). Another interesting finding is that the comparison methods SW and SWC are robust to noise from the outset, and the systematic error correction has only little effect or is even slightly counter-productive (compare method SWC, SWC in Fig. 15 (a), p. 44).

Finally, the robustness concerning the frequency variation of synthetic signals (Fig. 15, p. 44) and the overall robustness concerning natural signals (Fig. 22 (e), p. 46) show good agreement. Due to the different frequency and SNR regimes of the signal responses of different materials (Fig. 23, p. 47, Fig. 24, p. 47), the method's individual score varies remarkably. Nevertheless, the general picture is that the methods LAC, LRC and the literature-based comparison methods DH, DHC, SW, SWC deliver comparable robustness to frequency and noise.

Complexity. When automatically analysing thousands of signals or when implementing a method in a device with limited CPU power, the complexity of a method is of great concern. In this paper, that method metric refers to the computation time required to detect the primary wave's onset point and was measured in the course of the frequency variation of the sensitivity analysis.

As can be seen in Fig. 16, p. 44, the error correction generally has little impact on the complexity due to the simplicity of the systematic error correction approach (eq. 44, eq. 45). Furthermore, the Hilbert transformer used in method

DH and DHC is taking almost the same computation time as the linear regression used in method LR and LRC. For the methods SWC and SWC, the high computational effort, already addressed in the literature[18], is evident.

It is worth mentioning that optimising the detection parameters concerning the signal model requires considerable computational effort. However, if the signal model represents a signal class, the method's detection parameter optimisation only needs to be performed once for that signal class. Having optimised detection parameters, the detection is simple and works efficiently.

Accuracy and precision. Accuracy and precision are always of great concern when comparing different methods. Since the presented methods are particularly designed for the analysis of ultrasound signals, which come with a huge variety of frequencies and noise magnitudes, the assessment of precision ($\sim \mu$) and precision ($\sim \sigma$) is considering the worst case within the chosen ranges for frequency (eq. 10) and SNR (eq. 11). As can be seen in the results of the sensitivity analysis (Fig. 12, p. 41), that case appears for the lowest frequency ($\mathrm{F_{low}} = 5$ kHz) and the lowest SNR ($\mathrm{SNR_{low}} = 20$ dB) under consideration.

First, the results of the χ^2 homogeneity tests (Fig. 19, p. 45) clearly show that error distributions equal the normal distribution and thus equal the distribution type of the noise which causes the error. From that follows, that the detection methods do not introduce any systematic error except the bias related to the threshold values, which is reduced by error correction approach.

From the comparison of the method's accuracy and precision (Fig. 18, p. 45), it becomes apparent that the error correction of LAC and LRC results in a substantial increase in accuracy. In contrast, for the comparison methods DHC and SWC, the error correction has little effect. Furthermore, the signal's envelope employed by the methods DH and DHC is an improvement compared to the methods LA and LR, but has less effect than the error correction of the methods LAC and LRC.

Interestingly, the precision of the LAC, LRC, and DHC decreases due to error correction (Fig. 18, p. 45). That is because the estimated secant's gradient is subject to error due to noise. That error propagates in the systematic error correction (eq. 44), which refers to the already erroneous secant's gradient, thus increasing the standard deviation of the error distribution.

Performance. A convenient way to comparatively assess the performance of several methods is to conclude the most important method metrics in one number. Therefore, the method's performance is assessed by the composite performance score (see Fig. 20, p. 45) considering the normalised and inverted method metrics complexity C (Fig. 16, p. 44), accuracy A, and precision P (Fig. 18, p. 45). The overall score S_{CAP} considers all three method metrics, where the score S_{AP} does not include the metric complexity.

Obviously, the composite performance of method LRC is superior to all other methods, regardless of the complexity. If complexity does not matter, the comparison methods SW and SWC perform in the range of LA and LAC, but still less than LR.

It is essential to note that this comparison pertains to the worst-case scenario (low frequency, low SNR), which is a common situation when analysing ultrasound signals related to materials like cement paste. In such situations,

the desire for accuracy and precision often overshadows the computational effort. Furthermore, the detection error set used for the assessment relies on the predefined signal model parameters (eq. 3) and the corresponding detection parameters (see Tab. 5, p. 38), where other assumptions may yield different results.

Applicability domains. As already mentioned, the presented methods are designed for the analysis of ultrasound signals. But no method comes without limitations, specifically regarding frequency and noise.

In the materials section of this paper (see 5) specific ranges for frequency (eq. 10) and SNR (eq. 11) are defined as a basis for the entire analysis. Now it has to be shown whether these predefined ranges are reflected by natural signals from UPTM tests. As can be seen in the extreme values (minimum, maximum) of the frequency range estimates (Fig. 23 (e), p. 47) and SNR estimates (Fig. 24 (e), p. 47), the chosen value ranges show good agreement with the frequency and SNR estimates concerning different testing materials and measuring distances. The results for different testing materials differ considerably, emphasising the broad range of values to expect when analysing ultrasound signals.

Additionally, it is important to demonstrate that the proposed methods are not just applicable to a theoretical signal model but also to a variety of natural signals. As the exemplary analysis results show (Fig. 26, p. 62, Fig. 27, p. 63, Fig. 28, p. 64), the ultrasound signals[26] originating from cement paste tests exhibit such a variety in frequency and noise. The vast majority of those signals come with a high frequency, a low SNR and, therefore, small detection errors, which is as expected. Particular attention has to be paid to the signal recordings reflecting the material behaviour at the early stage of the cement paste's hydration process (0 to 300 minutes). In this time range, the frequency and the SNR drops while the detection error increases, which can also be observed in the results of the sensitivity analysis (Fig. 13, p. 42, Fig. 14, p. 43).

Equipped with these insights into the behavioural patterns of the presented detection methods it is now conclude the most important outcomes and to draw the attention to further improvements and possible applications.

5 Conclusion & Outlook

The final section of this paper summarises the conclusions regarding the assumptions, analyses and calculation results of the presented method comparison. Furthermore, the outlook is addressing possible applications and the potential for further improvement.

In terms of the investigated value ranges for the signal frequency (eq. 10) and SNR (eq. 11), and the chosen signal model $s[n, \theta)$ (eq. 2), the following conclusions can be drawn from the analysis results.

- Considering exceptions, it is possible to identify and parametrise a signal model that adapts well to the detection zone (the first ascending flank) of the primary wave's signal response. That allows for optimising the detection parameters concerning the signal model, paving the way for applying the optimised methods on natural signals.

- The signal model also adapts well to natural signals related to different test materials (cement paste, ambient air, tap water, aluminium cylinder). This circumstance suggests that the signal model not only represents a valid approximation for signals related to specific testing materials but also describes an entire class of ultrasound signals.
- The presented dual threshold detection methods utilise the signal model for detection parameter optimisation and systematic error correction. By approximating the signal in the detection zone with a secant and employing an error correction approach based on the secant's gradient, it is possible almost entirely to remove the bias due to the signal frequency. The residual onset point detection error is, therefore, almost entirely attributable to noise.
- The linear regression for estimating the signal's secant makes the method LRC a hybrid method consisting of dual threshold detection and regression analysis, where the regression analysis increases the robustness to noise. Regarding the regime of low frequency and low SNR, the method LRC exhibits the highest accuracy and precision among the presented methods and outperforms the adapted literature-based comparison methods DH, DHC, SW, and SWC. Due to the narrow range of signal amplitudes used for the regression analysis, the complexity of this method remains within affordable limits.

Future development. Possible applications of the presented methods are wherever a signal model is findable, which adapts well to the detection zone of the signal. However, the signal model and the detection methods were primarily designed for primary wave signal responses (compression wave) from ultrasonic pulse transmission tests. Since the signal responses of the secondary wave (a transversal wave) exhibit a similar signal shape in the detection zone, adapting the presented methods to secondary waves is worth testing.

Potential for further improvement. The potential for improvement lies primarily in identifying a well-suited signal model and expanding the application range to signals with a dominant noise-to-signal ratio (SNR $>$ 20 dB). It would be advantageous to have a method at hand that allows for automatic identification and parametrisation of a well-suited signal model. Due to the significant potential in pattern recognition, a machine-learning approach is a viable option. Furthermore, suitable signal preconditioning can increase the method's application range in terms of noise (SNR $\leq$ 20 dB). However, when considering low-pass filtering, the phase delay needs to be as small as possible, as this affects the shape of the signal and, therefore, the accuracy and precision of the time range estimates.

Expanding the scope of application. The detection and error correction approach described in this paper derives its advantageous effect solely from an innovative combination of well-known concepts from classic signal analysis. In particular, considering the signal's shape and the shape-related error correction enables a notable increase in robustness to frequency and noise, as well as accuracy and precision. Beyond ultrasound signals, it would be interesting to

investigate whether the proposed methods also perform well with signals from other sources.

Acknowledgements

The author of this paper conceived the entire analysis concept, implemented the source code used to compile the analysis results, designed and created all figures and tables, and wrote the entire manuscript.

The author declares that he has no known competing financial interests or personal relationships that could have appeared to influence the work reported in this paper. This research did not receive any specific grant from funding agencies in the public, commercial, or not-for-profit sectors.

Supported by TU Graz Open Access Publishing Fund.

References

Articles, Books

1. Palomar, Irene, Barluenga, Gonzalo, Varela, Hugo, Puentes, Javier & Rodríguez, A. *Non-Destructive Evaluation of Micro-Cracked SCC by Ultrasonic Waves* in (2020). https://doi.org/10.23967/dbmc.2020.101.
2. Mo, Shi, Jeong, Deok Hwa, Lee, Seung Woo & Choi, Yeol. Relationship Between UPV and Strength of Rubber-Concrete. *Defect and Diffusion Forum.* https://doi.org/10.4028/www.scientific.net/ddf.382.225 (2018).
3. Hadianfard, Mohammad Ali & Jafari, Saeed. Prediction of Lightweight Aggregate Concrete Compressive Strength Using Ultrasonic Pulse Velocity Test Through Gene Expression Programming. *Scientia Iranica.* https://doi.org/10.24200/sci.2016.2309 (2016).
4. Kumar, S. Application of Ultrasonic Techniques for Optimizing Dam Concrete Setting Process in Indian Construction Projects. *International Journal of Hydropower and Civil Engineering.* https://doi.org/10.22271/27078302.2023.v4.i1a.22 (2023).
5. Piechota, Piotr *et al.* Experimental Determination Influence of Flow Disturbances Behind the Knife Gate Valve on the Indications of the Ultrasonic Flow Meter With Clamp-on Sensors on Pipelines. *Sensors.* https://doi.org/10.3390/s23104677 (2023).
6. Synowiec, Piotr, Andruszkiewicz, A., Wędrychowicz, Wiesław, Piechota, Piotr & Wróblewska, Elżbieta. Influence of Flow Disturbances Behind the 90° Bend on the Indications of the Ultrasonic Flow Meter With Clamp-on Sensors on Pipelines. *Sensors.* https://doi.org/10.3390/s21030868 (2021).
7. Karimaei, Mahmood, Dabbaghi, Farshad, Dehestani, Mehdi & Rashidi, Maria. Estimating Compressive Strength of Concrete Containing Untreated Coal Waste Aggregates Using Ultrasonic Pulse Velocity. *Materials.* https://doi.org/10.3390/ma14030647 (2021).
8. Zouini, Rekia, Makani, Abdelkadir & Tafraoui, Ahmed. Investigation on the Mechanical Properties and Durability of High Performance Concrete Reinforced With Waste Tires Fibers. *The Journal of Engineering and Exact Sciences.* https://doi.org/10.18540/jcecvl9iss5pp16062-01e (2023).
9. Yee Yan, L., Scott, T. S. & Chee Kiong, S. Wave propagation based monitoring of concrete curing using piezoelectric materials: Review and path forward. *NDT & E International* **99,** 50–63. ISSN: 0963-8695. https://doi.org/10.1016/j.ndteint.2018.06.002 (2018).
10. Al-Qahtani, Saeed M., Wille, Marie-Luise & Langton, Christian M. Transducer Impulse Response Correction for a Deconvolution Derived Ultrasound Transit Time Spectrum. *Physics in Medicine and Biology.* https://doi.org/10.1088/1361-6560/aad8fb (2018).
11. Chen, Han Xin & Zuo, Ming J. Material Damage Ultrasonic Assessment by Time-of-Flight Estimation With an Adaptive Wavelet Filter. *Materials Science Forum.* https://doi.org/10.4028/www.scientific.net/msf.626-627.795 (2009).

12. Zahedi, Farshad, Yao, Jun & Huang, Haiying. A Passive Wireless Ultrasound Pitch–catch System. *Smart Materials and Structures.* https://doi.org/10.1088/0964-1726/24/8/085030 (2015).

13. Li, W., Chen, Q. & Wu, J. Double threshold ultrasonic distance measurement technique and its application. *Review of Scientific Instruments* **85,** 044905. ISSN: 0034-6748. https://doi.org/10.1063/1.4871993 (Apr. 2014).

14. Chang, Jin Ho, Zhou, Qifa & Shung, K. Kirk. Design and Implementation of High Frequency Ultrasound Pulsed-Wave Doppler Using FPGA. *Ieee Transactions on Ultrasonics Ferroelectrics and Frequency Control.* https://doi.org/10.1109/tuffc.904 (2008).

15. Piyush, Dhiman, Nitin, Kumar, Bishan, Yadav, Sanjay & Dubey, P. K. Measurement of ultrasonic pulse velocity with improved accuracy using automatic threshold error correction. *Review of Scientific Instruments* **94,** 045101. ISSN: 0034-6748. https://doi.org/10.1063/5.0142739 (Apr. 2023).

16. Wang, Mi, Zheng, Dandan, Mei, Jianqiang, Mao, Yang & Hu, Jiayu. A New Method for Processing Ultrasonic Gas Flowmeter Signal in Wet Gas. *Iet Science Measurement & Technology.* https://doi.org/10.1049/smt2.12001 (2020).

17. Hou, Hui-Rang, Zheng, Dandan & Nie, Laixiao. Gas Ultrasonic Flow Rate Measurement Through Genetic-Ant Colony Optimization Based on the Ultrasonic Pulse Received Signal Model. *Measurement Science and Technology.* https://doi.org/10.1088/0957-0233/26/4/045005 (2015).

18. Barshan, B. Fast processing techniques for accurate ultrasonic range measurements. *Measurement Science and Technology* **11,** 45. https://dx.doi.org/10.1088/0957-0233/11/1/307 (Jan. 2000).

19. Harden, J. *Experimental study on cement paste using the ultrasonic pulse transmission method* Engineering Archive. Mar. 2025. https://doi.org/10.31224/4465.

20. in. *Digital Communications with Emphasis on Data Modems* 752 (John Wiley & Sons, Ltd, 2017). ISBN: 9781119011866. https://onlinelibrary.wiley.com/doi/abs/10.1002/9781119011866.app2.

21. Oppenheim, Alan V., S. *Discrete-time signal processing* 2nd ed., 792. ISBN: 0137549202. https://research.iaun.ac.ir/pd/naghsh/pdfs/UploadFile_2230.pdf (Prentice Hall, Inc., 1999).

22. Harris-Birtill,David & Harris-Birtill, Rose. in *Time in Variance* 220–248 (Brill, Leiden, The Netherlands, 2021). ISBN: 9789004470170. https://doi.org/10.1163/9789004470170_014.

23. Franke, T., Ho, T. & Christie, C. A. The chi-square test. *American Journal of Evaluation* **33,** 448–458. https://doi.org/10.1177/1098214011426594 (3 2011).

24. Marsaglia, G. & Tsang, W. W. The ziggurat method for generating random variables. *Journal of Statistical Software* **5.** https://doi.org/10.18637/jss.v005.i08 (8 2000).

25. Freedman, D. A. & Diaconis, P. On the histogram as a density estimator:l 2 theory. *Zeitschrift Für Wahrscheinlichkeitstheorie Und Verwandte Gebiete* **57,** 453–476. https://doi.org/10.1007/bf01025868 (4 1981).

Data Records

26. Harden, J. *Ultrasonic Pulse Transmission Tests: Datasets – Test Series 1, Cement Paste at Early Stages* version 1.0. Graz University of Technology. https://doi.org/10.3217/bhs4g-m3z76.

27. Harden, J. *Ultrasonic Pulse Transmission Tests: Datasets – Test Series 5, Reference Tests on Air* version 1.0. Graz University of Technology. https://doi.org/10.3217/bjkrj-pg829.

28. Harden, J. *Ultrasonic Pulse Transmission Tests: Datasets – Test Series 6, Reference Tests on Water* version 1.0. Graz University of Technology. https://doi.org/10.3217/hn7we-q7z09.

29. Harden, J. *Ultrasonic Pulse Transmission Tests: Datasets – Test Series 7, Reference Tests on Aluminium Cylinder* version 1.1. TU Graz Repository. https://doi.org/10.3217/w3mb5-1wx17.

Online Resources

30. Harden, J. *Source code for: Enhanced threshold detection method enabling fast and robust primary wave time range estimation* version 1.0.0-beta1. Graz University of Technology. https://doi.org/10.3217/tthv9-6yx74.

31. Harden, J. *Supplementary analysis results for: Enhanced threshold detection method enabling fast and robust primary wave time range estimation* version 1.0.0-beta1. Graz University of Technology. https://doi.org/10.3217/5shdb-rhz09.

Appendix

In the Appendix section, one can find further detailed and/or exemplary analysis results. These are the optimised detection parameters concerning different testing materials (Tab. 6, p. 58, Tab. 7, p. 59, Tab. 8, p. 59, Tab. 9, p. 60), several visualisations of the curve-fitting results for single signals (Tab. 10, p. 60, Fig. 25, p. 61), and exemplary analysis results for different ultrasonic measuring distances related to test series 1 (cement paste, Fig. 26, p. 62, Fig. 27, p. 63, Fig. 28, p. 64).

Signal model parameters			
Parameter	α	β	γ
Value	2.12	0.05	0.7
Secant detection parameters			
Method	t_0	t_1	t_2
LA, LAC	0.560	0.200	0.920
LR, LRC	0.562	0.182	0.941
DH, DHC	0.587	0.391	0.782
SW, SWC	0.560	0.200	0.920
Sliding window parameters			
Method	t_v	t_w	
SW, SWC	0.500	0.347	
Error correction parameters			
Method	$t_{c,0}$	$t_{c,1}$	
LAC	0.666	−0.475	
LRC	0.717	−0.525	
DHC	0.035	−0.078	
SWC	0.000	−1.974	

Table 6: Detection parameters optimised concerning the signal fitting results of test series 1 (cement paste). *Legend:* t_0 ... initial threshold; t_1 ... lower threshold; t_2 ... upper threshold; t_v ... voltage threshold; t_w ... window fill threshold; $t_{c,0}$, $t_{c,1}$ ... monomial coefficients of the correction threshold polynomial $t_{c,\mathrm{app}}$; the number in the subscript refers to the monomial's power.

Signal model parameters			
Parameter	α	β	γ
Value	2.14	0.35	1.63
Secant detection parameters			
Method	t_0	t_1	t_2
LA, LAC	0.556	0.199	0.912
LR, LRC	0.557	0.182	0.932
DH, DHC	0.539	0.359	0.719
SW, SWC	0.556	0.199	0.912
Sliding window parameters			
Method	t_v	t_w	
SW, SWC	0.500	0.355	
Error correction parameters			
Method	$t_{c,0}$	$t_{c,1}$	
LAC	0.640	−0.383	
LRC	0.689	−0.527	
DHC	0.054	−0.063	
SWC	−0.000	−1.769	

Table 7: Detection parameters optimised concerning the signal fitting results of test series 5 (ambient air). *Legend:* see Tab. 6, p. 58.

Signal model parameters			
Parameter	α	β	γ
Value	1.84	0.15	1.74
Secant detection parameters			
Method	t_0	t_1	t_2
LA, LAC	0.559	0.202	0.917
LR, LRC	0.561	0.185	0.937
DH, DHC	0.536	0.357	0.715
SW, SWC	0.559	0.202	0.917
Sliding window parameters			
Method	t_v	t_w	
SW, SWC	0.500	0.350	
Error correction parameters			
Method	$t_{c,0}$	$t_{c,1}$	
LAC	0.652	−0.371	
LRC	0.702	−0.572	
DHC	0.081	−0.042	
SWC	−0.000	−1.658	

Table 8: Detection parameters optimised concerning the signal fitting results of test series 6 (tap water). *Legend:* see Tab. 6, p. 58.

Signal model parameters			
Parameter	α	β	γ
Value	1.74	0.12	0.83
Secant detection parameters			
Method	t_0	t_1	t_2
LA, LAC	0.563	0.203	0.923
LR, LRC	0.565	0.185	0.945
DH, DHC	0.579	0.386	0.772
SW, SWC	0.563	0.203	0.923
Sliding window parameters			
Method	t_v	t_w	
SW, SWC	0.500	0.343	
Error correction parameters			
Method	$t_{c,0}$	$t_{c,1}$	
LAC	0.673	−0.436	
LRC	0.724	−0.558	
DHC	0.153	−0.117	
SWC	0.000	−2.040	

Table 9: Detection parameters optimised concerning the signal fitting results of test series 7 (aluminium cylinder). *Legend:* see Tab. 6, p. 58.

Data set designation	SID	L_{det} [1]	E [$V^2 \cdot 10^3$]	R [1]	α [1]	β [1]	γ [1]
ts1_wc040_d50_5	288	18	0.012	0.9999	2.07	0.14	1.04
ts1_wc040_d50_5	50	85	0.006	1	2.27	0.3	0.68
ts1_wc040_d50_5	20	342	0.528	0.9966	1.9	0	0
ts5_d50_b16_v800	1	26	0.016	0.9999	2.03	0.79	2.15
ts6_d70_b16_v800	1	15	0.109	0.9993	1.81	0.11	1.06
ts7_d50_b16_v800	1	16	0.04	0.9998	1.6	0.12	0.97
ts6_d25_b16_v600	1	12	3.226	0.9852	2.09	0.71	1.49
ts6_d50_b16_v600	1	15	4.545	0.9764	1.64	0	0.5

Table 10: Exemplary curve-fitting results for selected signals. *Legend:* SID ... signal identifier; L_{det} ... optimisation interval length (samples); E ... residual fitting error (weighted metric score); R ... correlation coefficient. See also Fig. 25, p. 61.

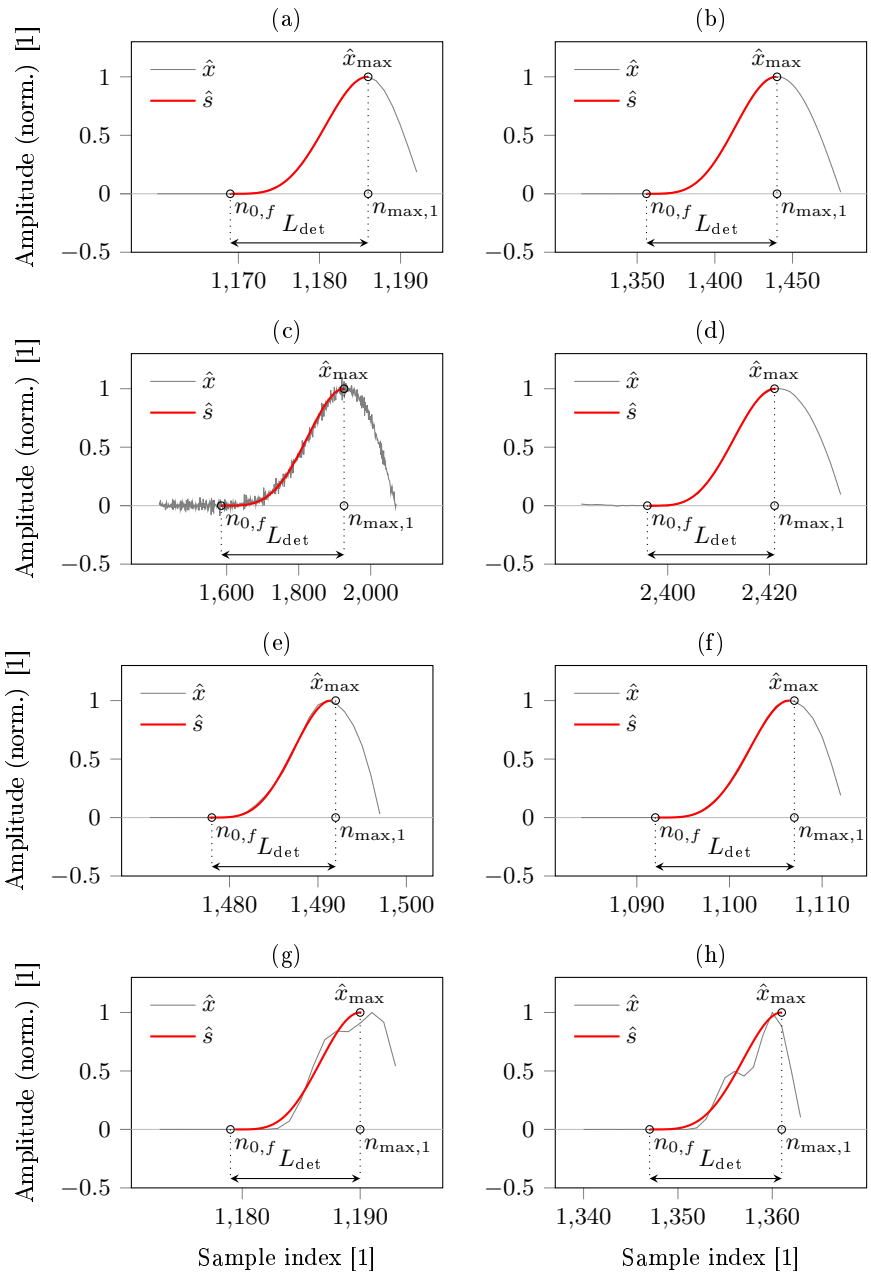

Figure 25: Exemplary curve-fitting results for selected natural signals. **(a)** cement paste, data set ts1_wc040_d50_5, SID 288. **(b)** cement paste, data set ts1_wc040_d50_5, SID 50. **(c)** cement paste, data set ts1_wc040_d50_5, SID 20. **(d)** ambient air, data set ts5_d50_b16_v800, SID 1. **(e)** tap water, data set ts6_d70_b16_v800, SID 1. **(f)** aluminium cylinder, data set ts7_d50_b16_v800, SID 1. **(g)** tap water, UMD 25 mm, data set ts6_d25_b16_v600, SID 1 (counterexample 1). **(h)** tap water, UMD 50 mm, data set ts6_d50_b16_v600, SID 1 (counterexample 2). See also Tab. 10, p. 60.

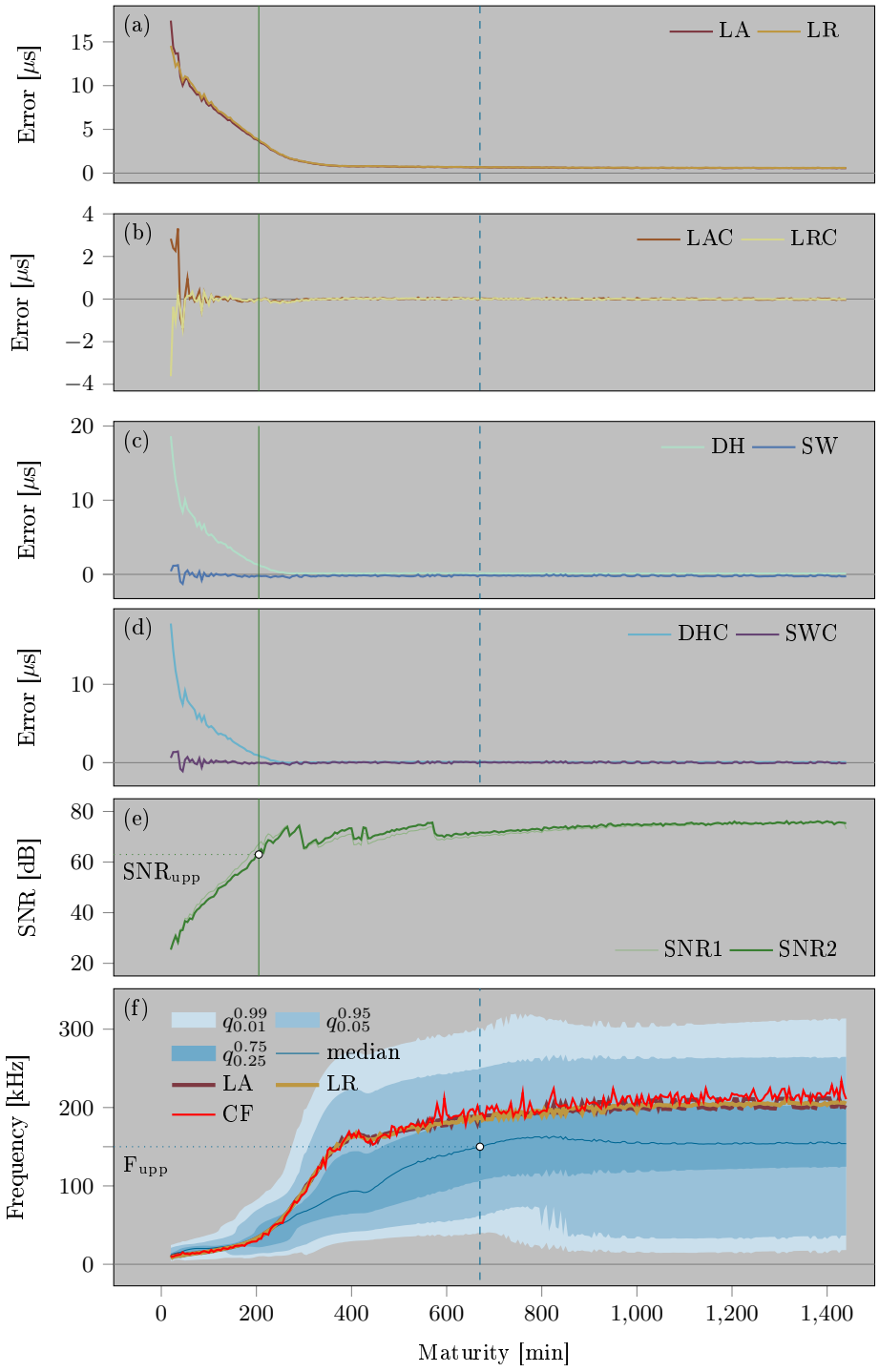

Figure 26: Onset point detection error, SNR and frequency range estimates. Cement paste within the first 24 hours after blending, measuring distance 25 mm, data set ts1_wc040_d25_5. **(a)** to **(d)** detection error. **(e)** SNR. **(f)** frequency. *Legend:* CF . . . curve-fitting.

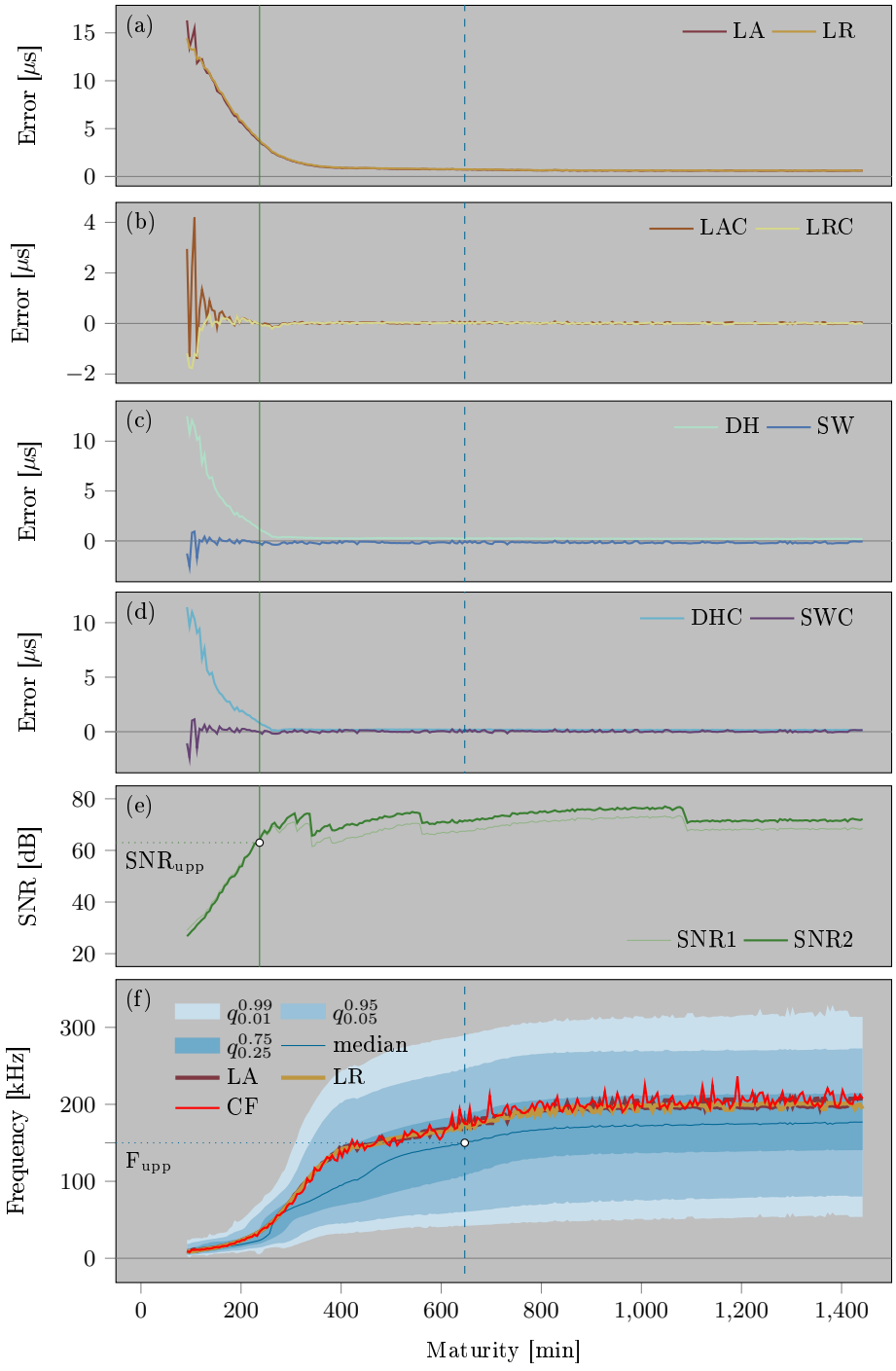

Figure 27: Onset point detection error, SNR and frequency range estimates. Cement paste within the first 24 hours after blending, UMD 50 mm, data set ts1_wc040_d50_5. **(a)** to **(d)** detection error. **(e)** SNR. **(f)** frequency. *Legend:* SF ... signal model fitting.

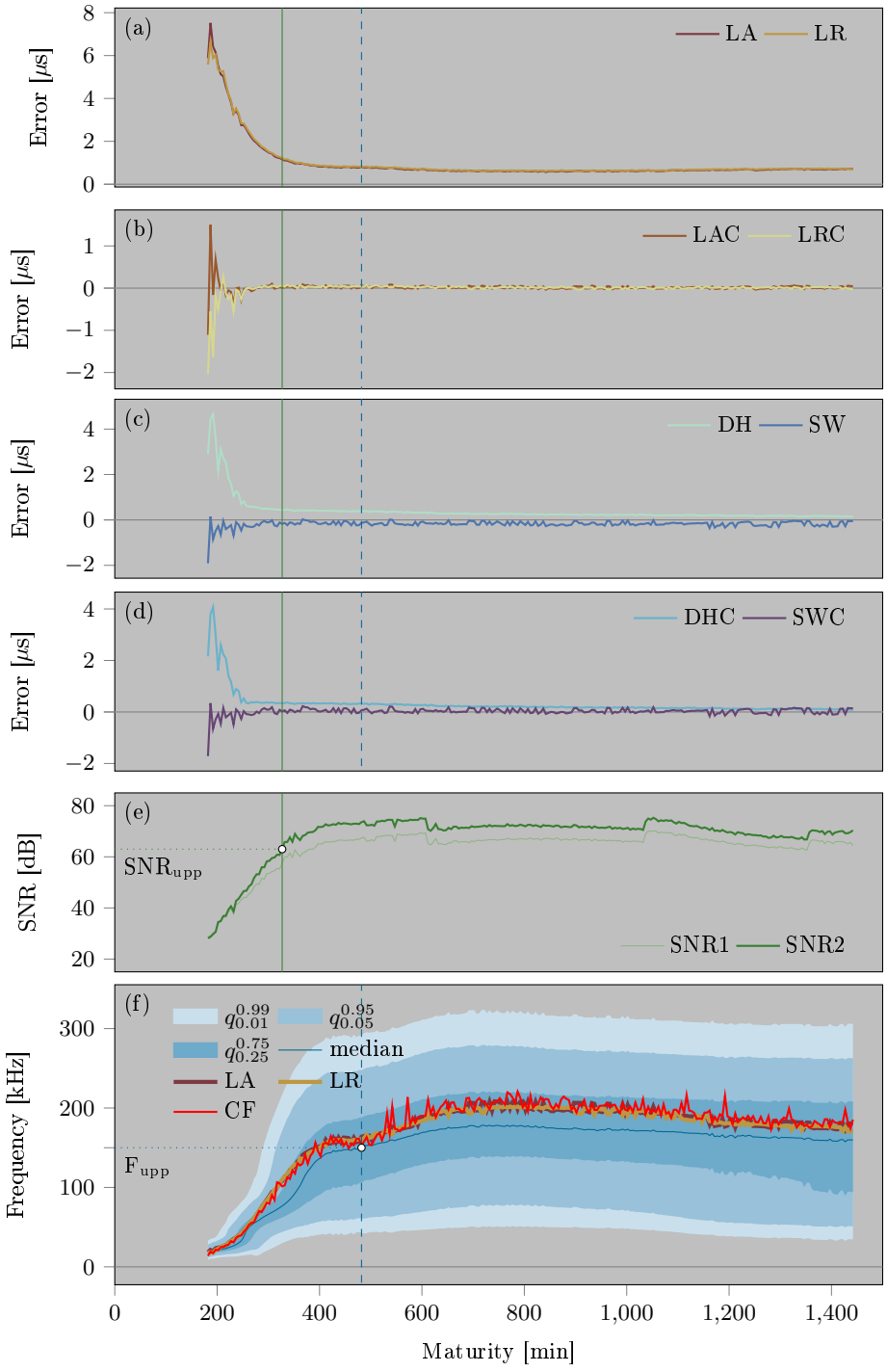

Figure 28: Onset point detection error, SNR and frequency range estimates. Cement paste within the first 24 hours after blending, measuring distance 70 mm, data set ts1_wc040_d70_5. **(a)** to **(d)** detection error. **(e)** SNR. **(f)** frequency. *Legend:* SF . . . signal model fitting.